ALICE DCal: An Addendum to the EMCal Technical Design Report

Di-Jet and Hadron-Jet correlation measurements in ALICE

The ALICE Collaboration

and

J. Allen,[6] C. Bernard,[7] O. Bourrion,[7] M. Chala,[7] M. Del Franio,[6] O. Driga,[8] F. Fichera,[3] N. Giudice,[4] A. Grimaldi,[3] P. Laloux,[8] Q. Li,[5] F. Librizzi,[3] G. Liu,[9] C. Loizides,[1] G. Marcotte,[7] S. Muggeo,[7] J-F Muraz,[7] F. Noto,[4] A. Orlandi,[6] V. Petrov,[5] F. Pompei,[5] W. Qian,[9] J. Rasson,[1] S. Sakai,[1] M. Salemi,[3] M. Sharma,[5] V. Sparti,[3] J-S Stutzmann,[8] A.Timmons,[5] A. Viticchie',[6] M. Wang,[9] X. Xiang,[9] F. Zhang,[9] J. Zhou,[2] X. Zhu, [9]

June 20, 2010

CERN-LHCC-2010-011 / ALICE-TDR-014-ADD-1
20/06/2010

1. Lawrence Berkeley National Laboratory, Berkeley
2. China Institute of Atomic Energy (CIAE)
3. Istituto Nazionale di Fisica Nucleare, Sezione di Catania
4. Dipartimento di Fisica dell Università Catania, Sezione INFN
5. Department of Physics and Astronomy, Wayne State University, Detroit
6. Istituto Nazionale di Fisica Nucleare, Laboratori Nazionali di Frascati
7. LPSC University Joseph Fourier Grenoble I, CNRS-IN2P3
8. SUBATECH, Ecole des Mines de Nantes, University de Nantes, CNRS-IN2P3
9. Huazhong Normal University (CCNU), Wuhan

Table of Contents

I. Introduction

The Large Hadron Collider (LHC) at CERN Laboratory in Geneva, Switzerland is opening a new high-energy frontier in the physics of hot QCD matter and the Quark Gluon Plasma (QGP). This addendum to the ALICE Electromagnetic Calorimeter (EMCal) Technical Design Report (TDR), describes an extension of the scope of the ALICE EMCal specifically designed to extend the acceptance of the EMCal and allow the measurement of hadron-jet and di-jet correlations. To distinguish it from on-going work on the EMCal, this extended electromagnetic calorimeter acceptance is designated the ALICE Di-Jet Calorimeter (ALICE-DCal). This addendum comes at a time when the larger project to construct a single-arm electromagnetic calorimeter for ALICE (EMCal) is in its final construction stage. As discussed in the following, the DCal expands the physics capabilities of the EMCal by enabling back-to-back correlation measurements, which are impossible with the EMCal alone, but are essential to obtain a complete picture of the physics addressed by the EMCal.

Together, the DCal and EMCal form a two-arm electromagnetic calorimeter. The EMCal subtends 110^o and the DCal subtends 60^o in ϕ, with both detectors covering $|\eta| < 0.7$, thereby providing good acceptance for di-jets with radii $R \leq 0.4$ up to transverse momenta $p_T \sim 150$ GeV/c. The physics case for the DCal and supporting simulations are discussed in Chapter II.

The EMCal portion of this two-arm spectrometer uses a contiguous set of 10 EMCal super modules. The DCal portion uses 6 super modules of the EMCal design with reduced length (in the η direction) in conjunction with 3 super modules of the existing PHOS electro-magnetic calorimeter. This configuration is discussed in detail in Chapter VI.

Simulation studies of the DCal have been carried out and have verified that the technology originally developed for and implemented in the EMCal will meet all the needs of the DCal project. As a consequence, from a technical perspective, the DCal is merely an extension of the EMCal construction effort. The full EMCal collaboration is participating in the DCal project. In addition, new scientific and technical expertise has been added to the collaboration from China (led by Wuhan) and Japan (led Tsukuba).

This document describes the DCal detector, the physics that it addresses, the cost and schedule and the project organization.

II. The Physics of DCal in ALICE

II.1. Overview

The DCal will extend significantly the jet quenching measurements enabled by the EMCal in ALICE, by providing large acceptance for back-to-back correlation measurements of jets and hadrons. The EMCal has superb capabilities for inclusive jet measurements (ALICE EMCal Physics Performance Report, 2009[1]). However, experience with jet quenching measurements at RHIC has shown that the combination of inclusive and correlation measurements is a much more powerful probe of jet quenching than inclusive measurements alone. Addition of the DCal in ALICE makes hadron+jet and jet+jet correlation measurements possible at high statistics over a very broad kinematic range, thereby expanding ALICE physics capabilities significantly.

The most significant measurements enabled by the DCal, and those which are the focus of this discussion, are as follows:

- the correlation of a jet recoiling back-to-back from a triggered high p_T π^0 exploits the phenomenology of jet quenching to provide a unique geometric bias, maximizing the path length of the recoiling jet in the hot medium. In one heavy ion running year (0.5 nb^{-1} for Pb+Pb) the DCal and EMCal will measure several thousand fully reconstructed jets with energy greater than 150 GeV recoiling from a π^0 trigger with $p_T > 20$ GeV/c.
- the DCal and EMCal will measure the correlation of fully reconstructed jet pairs with large cone radius ($R \sim 0.4$), with 1000 counts above $E_T \sim 140$ GeV. This likewise enables unique jet quenching measurements, for instance the study of energy balance between recoiling jet pairs.

This section presents the physics case for addition of the DCal, using simulations of several possible physics signals. This is not an exhaustive list of all measurements the DCal will carry out, but rather a representative set that illustrates its physics reach. We estimate jet quenching effects utilizing the qPYTHIA Monte Carlo model, which is the only model currently available that incorporates a theoretically well-motivated quenching mechanism.

II.2 Background from RHIC

Figure II.1 shows two well-known RHIC measurements of jet quenching, exploiting the azimuthally back-to-back nature of QCD jet production at leading order. The left panel shows the azimuthal separation of hadron pairs in 200 GeV p+p, d+Au and central Au+Au collisions, with "trigger" hadron having $p_T > 4$ GeV/c and associated hadron $p_T > 2$ GeV/c (Adams, J. et al. (STAR Collaboration) 2003). Focusing on the recoil direction ($\Delta\phi \sim \pi$), significant correlation strength above uniform background is seen for the more elementary collisions (p+p, d+Au), consistent with di-jet production, but strong suppression of the

[1] See EMCal_ppr.pdf at http://rhic23.physics.wayne.edu/~cormier/

correlation is observed for central Au+Au collisions. This is a dramatic and unambiguous signature of jet quenching.

Note, however, that the correlation in the left panel is measured only for hadrons with $p_T > 2$ GeV/c. The observed suppression does not mean that jets are completely absorbed – total jet energy and momentum must be conserved, regardless of interactions with the medium. Rather, it indicates that jet fragmentation has been markedly softened, with the bulk of the jet energy carried by hadrons below the kinematic cutoff. This picture is supported qualitatively by correlation measurements with much lower p_T cutoff for the associated hadron.

The right panel shows a similar di-hadron correlation analysis, but with larger kinematic cuts than the left panel (Adams, J., et al. (STAR Collaboration) 2006). The trigger hadron has $p_T > 8$ GeV/c in all cases, while the bottom sub-panels show the azimuthal correlation for associated $p_T > 6$ GeV/c. In this case even for the most central Au+Au collisions there is finite recoil correlation strength, though at markedly lower correlation rate (factor ~5) than for the d+Au reference measurement, and with no evident azimuthal broadening of the recoil peak. Model calculations indicated that this "punch-through" component has a contribution from di-jets generated at the surface of the fireball and oriented tangentially, so that both escape with minimal interaction. There is also a finite probability that both jets producing the di-hadron originate in the core and emerge without medium-induced radiation, because QCD bremsstrahlung is suppressed at very low gluon energy and the energy lost due to interactions is radiated into a few gluons with typical $p_T \sim 1$ GeV/c.

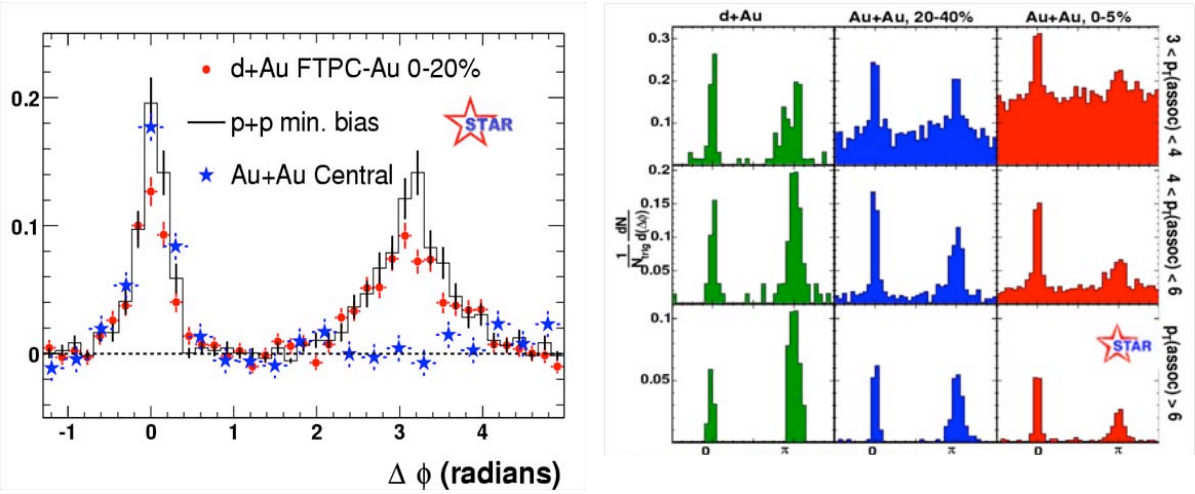

Figure II.1 High p_T hadron correlation measurements of jet quenching (Adams, J. et al. (STAR Collaboration) 2003), (Abelev, B. I. et al. (STAR Collaboration) 2006).

These analyses show the unique capabilities of correlation measurements to probe the physics underlying jet quenching, but also the limitations introduced by constraining measurements to hadronic observables. Jet quenching is by its nature a partonic process, and

full jet reconstruction will make a closer connection to the dynamics of jet quenching at the partonic level. First attempts at full jet reconstruction in the heavy ion collision environment have been carried out by the STAR collaboration (M. Ploskon (STAR Collaboration) 2009)(E. Bruna (STAR Collaboration) 2009).

Figure II.2 shows a correlation measurement from these studies, in this case a hybrid hadron+jet correlation (M. Ploskon (STAR Collaboration) 2009). The techniques for quantitative analysis of full jet reconstruction in a high background environment are complex, and are discussed in the above references and (ALICE EMCal Physics Performance Report, 2009). The measurement is similar to that in Figure II.1, right panel, but with the "associated hadron" replaced by a recoiling, fully reconstructed jet. This hybrid hadron+jet measurement is of interest precisely because of the strong geometric bias generated by a hadron trigger when jet quenching is large. We have mentioned above the bias towards a non-interacting jet population induced by a high p_T hadron trigger. We put that bias to use in this measurement: the stronger the surface bias of the trigger, the greater the path length in the dense medium of the recoiling jet at opposite azimuth. By reconstructing the full jet on the recoil side, rather than asking for another high p_T hadron as in Figure II.1, we can make a much more comprehensive study of jet interactions in matter.

We can tune the geometry of jet propagation in the fireball yet more finely by imposing additional biases on the measurement, by requiring that the leading hadron in the recoil jet be above some threshold, as illustrated in the illustrations in the left panel of Figure II.2. A high threshold for the recoil jet leading hadron corresponds directly to the measurement in Figure II.1, right panel, but now with a jet built around the recoil.

Figure II.2, right panel shows the ratio of correlation yields in such measurements, for central Au+Au collisions divided by that for p+p collisions (M. Ploskon (STAR Collaboration) 2009). The correlation yield is defined as the observed number of jets at a given E_T normalized by the number of *hadron pair* triggers. Suppression of the ratio below unity indicates loss of recoil jet yield, due to quenching.

Figure II.2 shows that the highly biased recoil jet population with hard leading hadron (black) is fully reconstructed in heavy ion collisions, whereas the unbiased population, with effectively no fragmentation constraint on the recoil jet, is strongly suppressed at high E_T. Since jet reconstruction requires a finite cone radius R (=0.4 in this case), such suppression must be due to strong broadening of the energy profile of the jet in matter. Inclusive jet measurements likewise point in this direction (M. Ploskon (STAR Collaboration) 2009).

A consistent picture of jet broadening due to quenching is emerging from the combined analysis of inclusive and correlation measurements of fully reconstructed jets. These measurements have garnered significant theoretical attention, with many theory groups now trying to understand the broadening based on analytical calculations of quenching, or the modification of Monte Carlo event generators (PYTHIA, HERWIG) to incorporate quenching effects.

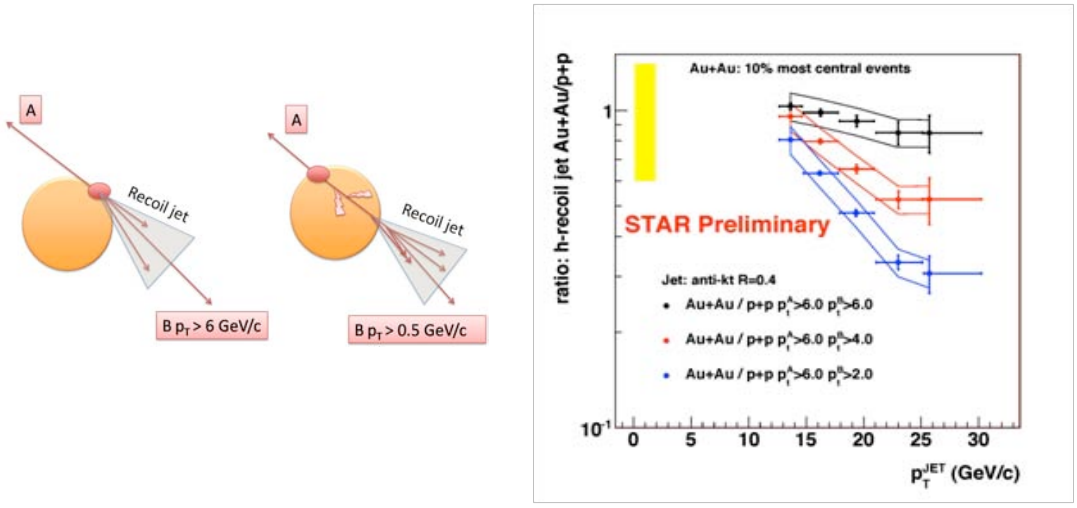

Figure II.2 Hadron+jet correlations in 200 GeV central Au+Au collisions (M. Ploskon (STAR Collaboration) 2009).

II.3 DCal Physics

The RHIC studies presented in the previous section show the detail with which the physics of jet quenching can be probed by correlation measurements. Kinematic reach will be vastly greater at the LHC, and we now present the major capabilities for jet measurements in ALICE that will be enabled by addition of the DCal. We concentrate on those measurement channels where the DCal brings qualitatively new physics, namely triggered hadron+jet and jet+jet correlations. Inclusive measurements of π^0, photons, and non-photonic electrons from heavy flavor will also be enhanced by the DCal, However, their rates scale linearly with acceptance and the improvement brought by the DCal relative to existing ALICE capabilities is not as significant as that for correlation measurements, thus we discuss them only briefly in this document.

We present several classes of simulations, to explore the physics capabilities of the DCal:

A. Event generator: qPYTHIA
B. Detector-Level simulation: detailed Geant model of the ALICE detector and DCal, for studying the instrumental response of DCal.
C. Particle-Level simulation: only detector acceptance is considered, with interactions in material. Detector response is approximated by utilizing only charged hadrons and photons (including decay photons from π^0 etc.) from the generator.

Event generation

We utilize the qPYTHIA model (N. Armesto, 2009) to investigate the effects of jet quenching. This is a modification of the standard PYTHIA Monte Carlo code, introducing Salgado-Wiedemann quenching weights in the parton shower and calculating the path length in medium using realistic nuclear geometry. Calculations are carried out at $\sqrt{s_{NN}}$ = 5.5

TeV for various values of quenching parameter qhat. While nuclear geometry is properly taken into account in calculating quenching weights, the qPYTHIA output is given in terms of p+p-equivalent cross sections. Rate estimates for Pb+Pb running are determined by scaling these cross sections by A^2x0.5 nb^{-1} corresponding to one LHC heavy ion running year for unbiased Pb+Pb collisions.

The results of qPYTHIA were compared to RHIC hadron and jet measurements (see ALICE EMCal Physics Performance Report, 2009[2]). That comparison showed that the current qPYTHIA version has limited precision in model quenching measurements; however, it is the only tool presently available, and we utilize it to give a sense of the possible magnitude of quenching effects. Improved Monte Carlo models are urgently needed for such studies, and for physics analysis of heavy ion data. This issue is receiving significant attention in the theory community, and members of the ALICE EMCal/DCal team are working actively with theorists in this area.

Detector geometry

The DCal is situated immediately adjacent to the PHOS on both the ALICE "A" and "C" sides. PHOS is an existing high granularity lead-tungstate electromagnetic calorimeter. We consider DCal+PHOS to be one integrated detector system for the study of jets, and all simulations include PHOS as well as DCal super modules (when we refer below to "jets in DCal" we always mean "jets in DCal super modules + PHOS", preferring the former for brevity). There will be a small gap between the sensitive volumes of DCal and PHOS, whose effect on jet measurements we investigate below.

Jet reconstruction

Jet reconstruction is carried out using the FastJet anti-k_T algorithm R=0.4 (see ALICE EMCal Physics Performance Report, 2009 for details), utilizing EM energy measured by EMCal or DCal+PHOS, and charged hadron energy measured by the ALICE tracking system. All references to "jet energy" refer to the measurement of the full jet energy, utilizing both calorimetry and tracking. Inclusive and correlation rates for jet measurements are reported only for jets fully contained within the acceptance of the EMCal or DCal+PHOS.

Trigger

An essential capability for the measurement of rare processes in ALICE is a fast and efficient trigger. The trigger architecture and capabilities of the DCal will be identical to those of the EMCal, both for EM showers (small clusters of towers due to high p_T γ, π^0, η, electrons, etc.) and for larger area jets. The EMCal Trigger architecture and physics performance are described in the ALICE EMCal Physics Performance Report, 2009 and the technical details are described in the ALICE EMCal TDR (LHCC-2008-14). In this proposal we assume that the DCal trigger is 100% efficient and unbiased for the channels under discussion; a more nuanced understanding requires detailed simulations.

[2] See EMCal_ppr.pdf at http://rhic23.physics.wayne.edu/~cormier/

II.3.1 Inclusive rates

For reference we first present inclusive rates for π^0, jets, photons and electrons. The DCal effectively increases the ALICE calorimeter acceptance for all of these observables (except large area jets) by a factor (10+6)/10~1.6, so inclusive rates are simply increased by 60%.

Figure II.3 shows the expected yield in one heavy ion running year for inclusive π^0 (left) and for jets (right). Addition of the DCal increases the π^0 kinematic reach by ~10 - 20 GeV/c for a given statistical precision. The inclusive jet is increased by a smaller factor (~20%), due to finite jet size.

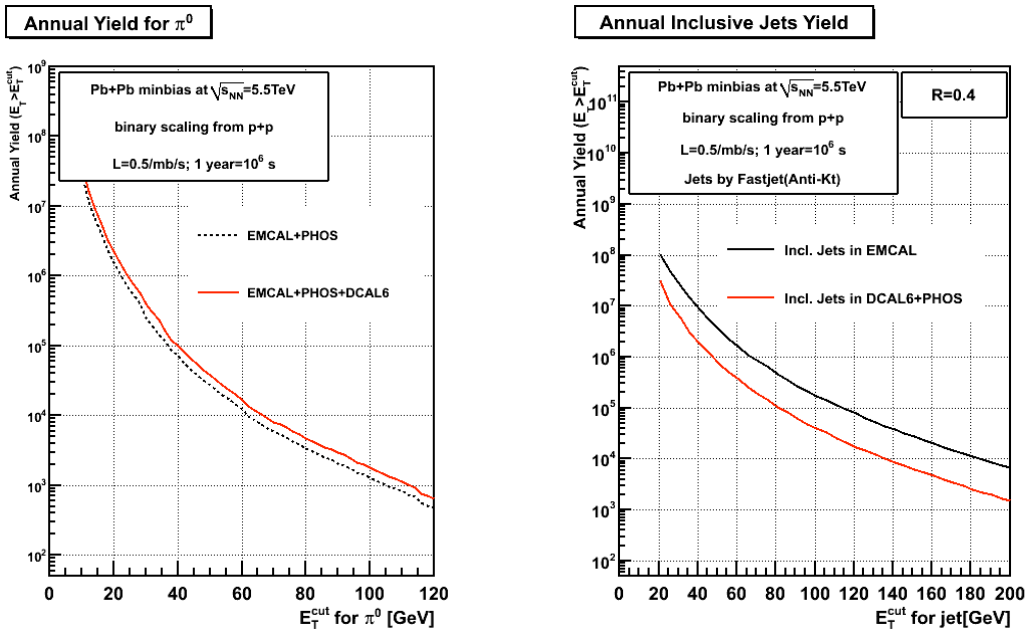

Figure II.3 Inclusive annual yields (integrated counts above a threshold) for 5.5 TeV Pb+Pb collisions. Left: π^0 in EMCal+PHOS only and in EMCal+PHOS+DCal . Right: inclusive jet rates in EMCal and in DCal+PHOS**.**

Figure II.4 shows the annual yields for inclusive prompt photons and electrons from B and W decay. The DCal enhances the statistics for these measurements by 60%, or equivalently increases the kinematic reach by a few GeV for a given statistical precision. While the improvement in statistics or kinematic reach for these channels due to DCal is modest, it should also be noted that there is significantly less material in front of the DCal than the EMCal since the TRD is not present at that azimuth. This arrangement was intended initially to minimize material in front of the PHOS for precision photon measurements at low p_T, but it will also benefit electron and photon measurements in the DCal. The effect of TRD material on electron measurements in the EMCal is under intensive study (ALICE EMCal Physics Performance Report, 2009), but the very low material budget in front of DCal will provide additional tools for high precision electron measurements and for understanding the systematic effects of the TRD on the EMCal (with TRD) measurements.

Since the rates for correlation measurements with a prompt photon or non-photonic electron as trigger are small, we do not consider such correlations further in this proposal.

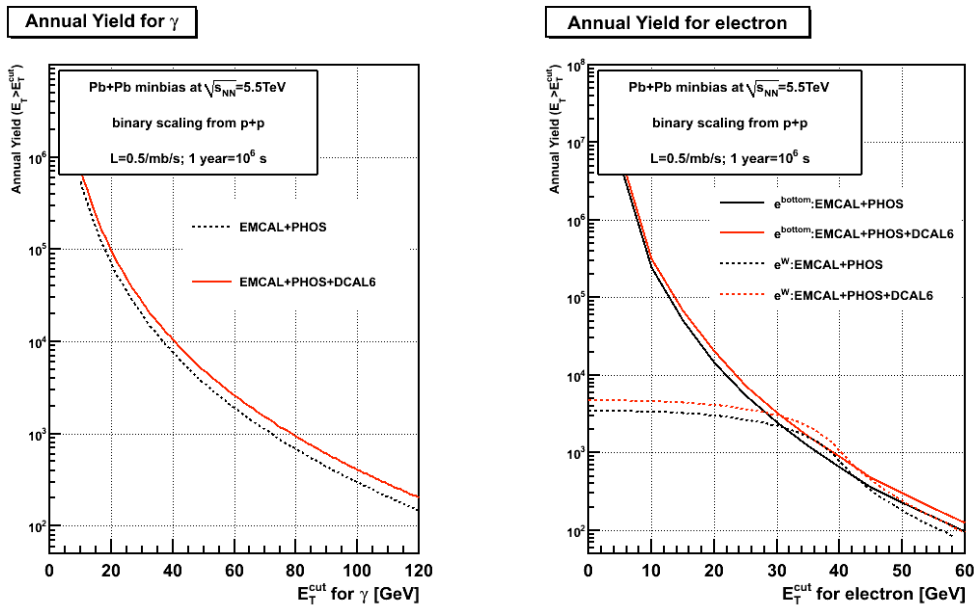

Figure II.4 Inclusive annual yields for 5.5 TeV Pb+Pb collisions. Left: prompt photons in EMCal+PHOS only, and in EMCal+DCal+PHOS. Right: electrons from B and W decays.

II.3.2 DCal Jet Energy Resolution

Figure II.5 shows the comparison of jet energy resolution in DCal and EMCal, for jets with $p_T \sim 90$ GeV/c. The simulation compares Particle and Detector Level jet energies on a jet-wise basis in each detector.

For complete jet energy analysis, correction must be made for double counting of electron and charged hadron energy (ALICE EMCal Physics Performance Report, 2009), which is measured both as charged particle tracks and as showers in the calorimeters. Accurate correction for this effect requires good matching between the projection of a charged particle trajectory and a DCal shower; however, for technical reasons this matching was not available for these simulations. We therefore do not apply this correction to either the EMCal or DCal jet energy measurement, allowing us to compare them on a fully consistent basis.

The instrumental jet energy resolution for DCal and EMCal is shown in Figure II.5. The instrumental resolution is defined as transverse momentum difference Δp_T for jets in the same Monte Carlo event, where the instrumental response is simulated alternatively at the detector level (full geant simulation) or the particle level (Monte Carlo generator output only). Jets are generated with PYTHIA in a narrow interval around $p_T^{MC} \sim 90$ GeV/c. Jet reconstruction uses FASTJET anti-k_T algorithm with R = 0.2. The jets are fully contained in the DCal acceptance, excluding PHOS and gap (red triangles) or the EMCal acceptance (open black stars). The instrumental resolution of DCal and EMCal are in good agreement, demonstrating that the extensive systematic studies reported in the EMCal PPR can also be utilized for DCal analysis.

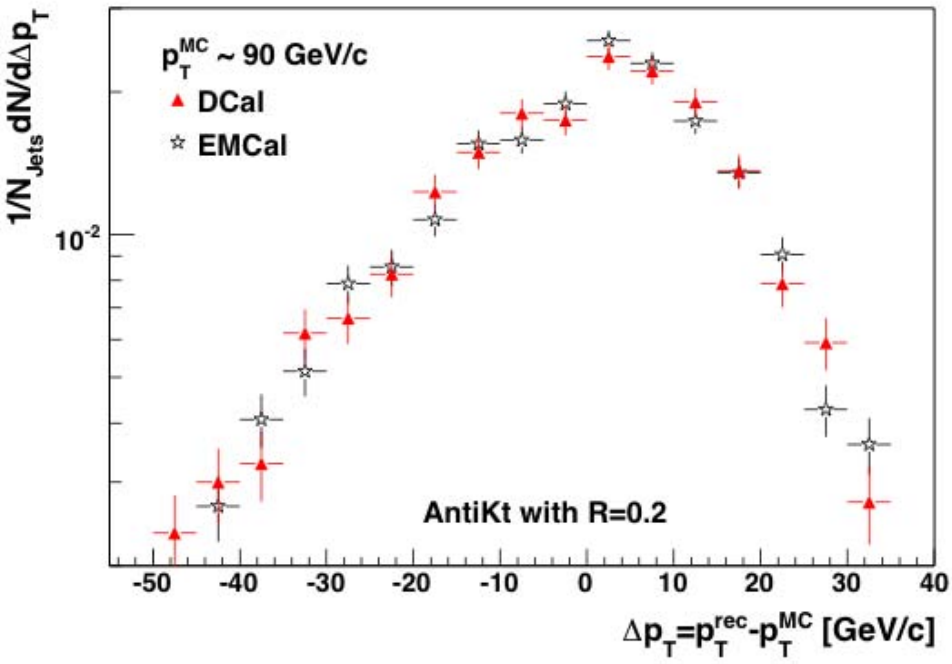

Figure II.5 Instrumental energy resolution ($\Delta p_T = p_T^{rec} - p_T^{MC}$, see text) for PYTHIA jets with $p_T^{MC} \sim 90$ GeV/c, fully reconstructed with anti-k_T algorithm and R = 0.2 in the DCal, excluding PHOS and gap (red triangles) and EMCal (open stars) acceptances.

II.3.3 Effect of PHOS-DCal gap

Unavoidably, there is some gap in η between the sensitive volumes of DCal and PHOS, due to the Super Module structure. The PHOS cryogenic utilities and other services will be reconfigured to minimize this gap, which may be as small as 10 cm, i.e. less than the width of one DCal module after these modifications are made. In terms of phase space, such a gap corresponds to $\delta\eta \sim 0.02$.

Figure II.6 shows the effect of the gap on a physics observable, the energy balance between a jet triggered in the EMCal and an azimuthally back-to-back recoil jet in the DCal. Simulation is at the Particle Level, for 5.5 TeV p+p collisions (the effect of quenching on di-jet energy balance is reported in the next section). Jets are measured using anti-kT with R = 0.4 in both calorimeter acceptances. The left panel shows the relative energy resolution of the jet pair, expressed as $\Delta = (E_T^{DCal}-E_T^{EMCal})/0.5*(E_T^{DCal}+E_T^{EMCal})$, with trigger threshold in EMCal requiring $E_T^{EMCal} > 90$ GeV. Note that the threshold (trigger) is imposed on the total jet energy in the EMCal acceptance, meaning that backgrounds in the DCal will cause the value of Δ to be negative.

The figure shows the recoil jet energy distribution in the DCal, for various values of the gap, including no gap, and for recoiling jets reconstructed solely from charged particle tracking (i.e. no DCal). For all but the charged-only distribution, a clear peak is seen in the vicinity of $\Delta \sim 0$, corresponding to the real back-to-back di-jet pair. A long tail to the left (i.e. small E_T^{DCal}) is seen, corresponding to the escape of the true recoil jet out of the acceptance and the reconstruction of a background jet instead. Statistical error bars correspond to 0.5 nb^{-1} Pb+Pb (for clarity no quenching effects have been imposed), which is also the statistical precision achievable in one running year of p+p at 5.5 TeV.

To quantify the di-jet energy resolution, we fit the peak near $\Delta \sim 0$ with a truncated Gaussian function, as shown by the solid lines in the figure. The right panel shows the dependence of the width extracted from this fit on the jet energy threshold in the EMCal. Above 100 GeV, the resolution is seen to be around 20%, and improves with increasing energy. This resolution is in agreement with the jet energy resolution for the EMCal alone, calculated in a different way by comparing Particle and Detector Level simulations. A gap between DCal and PHOS that is less than 20 – 40 cm is seen to have small impact on the measured di-jet energy resolution.

Figure II.6 also shows the di-jet energy balance for the configuration without the DCal, where the recoil jet energy is measured solely by charged particle tracks (pink). In this case no clear di-jet peak in the recoil distribution is seen (left panel), and fitting to the leading tail (right panel) generates resolution poorer than 30%. This is not a competitive measurement, thus this observable would not be accessible to ALICE without the DCal.

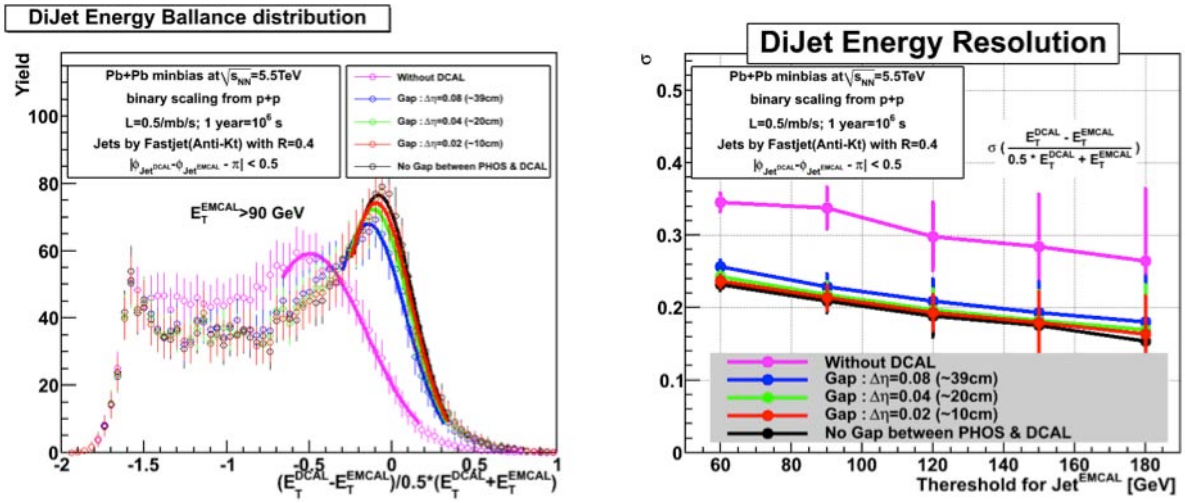

Figure II.6 Effect on jet energy resolution of gap between DCal and PHOS, measured by the di-jet energy balance in EMCal and DCal (anti-kT, R = 0.4 for both EMCal and DCal). Left: correlation for EMCal Trigger Jet E_T > 90 GeV, for no gap (black), various values of gap width (red, green, blue), and no DCal (charged tracking only, pink). Right: dependence of peak width on EMCal threshold E_T. Statistical error bars correspond to 0.5 nb^{-1} Pb+Pb, though for clarity no quenching effects have been imposed. This is the same statistical precision that will be achieved in one running year of p+p at 5.5 TeV.

II.3.4 Jet quenching measurements with DCal

II.3.4.1 Di-jet energy balance

We now turn to investigation of jet quenching observables with the DCal, beginning with the energy balance observable $\Delta = (E_T^{DCal}-E_T^{EMCal})/0.5*(E_T^{DCal}+E_T^{EMCal})$, for an azimuthally back-to-back jet pair. Note that the definition Δ is the same as in the previous section but in this case the threshold (trigger) is imposed on the DCal energy, so that the effect of backgrounds in the EMCal will be to cause the value of Δ to be positive.

Figure II.7 shows the distribution of Δ for azimuthally back-to-back di-jet pairs for strong quenching (qhat = 50 GeV^2/fm), with a trigger threshold imposed on the DCal jet energy of $E_T^{DCal} > 100$. The error bars show the statistical precision achievable in this observable for central collisions of 5.5 TeV Pb+Pb at 0.5 nb^{-1}. The peak near Δ~0 corresponds to the true di-jet pairs, whereas the tail (to positive Δ) is due to events in which the recoil jet escapes the acceptance and a jet from the event background is reconstructed instead.

The solid lines show fits of Gaussian functions, truncated to the region dominated by the true di-jet pairs. There is some arbitrariness to the choice of fit region, whose systematics will be investigated with real data.

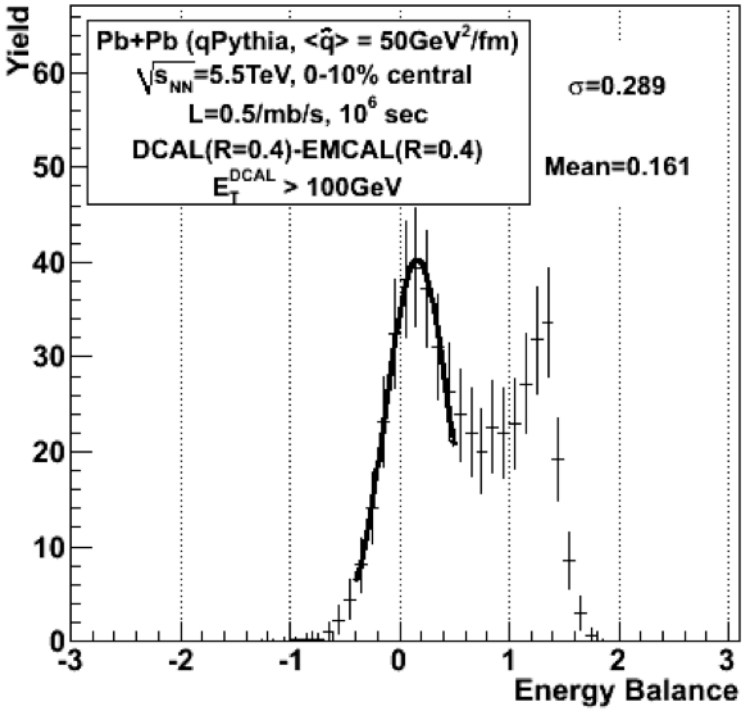

Figure II.7 Distribution of di-jet energy balance Δ for quenched jets (qhat = 50 GeV^2/fm), for DCal jet energy threshold of 100 GeV. Error bars show the statistical precision of the signal for 0.5 nb^{-1} of 5.5 TeV Pb+Pb (0-10% central collisions). Solid line represents a fit to a truncated Gaussian function.

Figure II.8 shows the dependence of the fitted width and centroid shift of the truncated Gaussian function on the DCal jet energy threshold for highly quenched jets (qhat=50 GeV^2/fm, red stars) and unquenched jets (qhat=0, black circles). The error bars show the effect of finite statistics on the fit parameters, corresponding to 0.5 nb^{-1} of Pb+Pb collisions. The broadening of the recoil jet energy distribution, and the loss of energy due to quenching (corresponding to positive Δ), are seen to be measurable with good statistical precision up to $E_T^{DCal} \sim 150$ GeV. This measurement serves as a complement to γ+hadron measurements, but with different physics emphasis and much greater kinematic reach. In this case, the measurement utilizes the trigger jet to fix (approximately) the Q^2 of the interaction, and studies the broadening and energy loss of the recoil jet. This is a new observable which has not yet received theoretical attention. However, its importance is clear, and it cannot be carried out without the DCal.

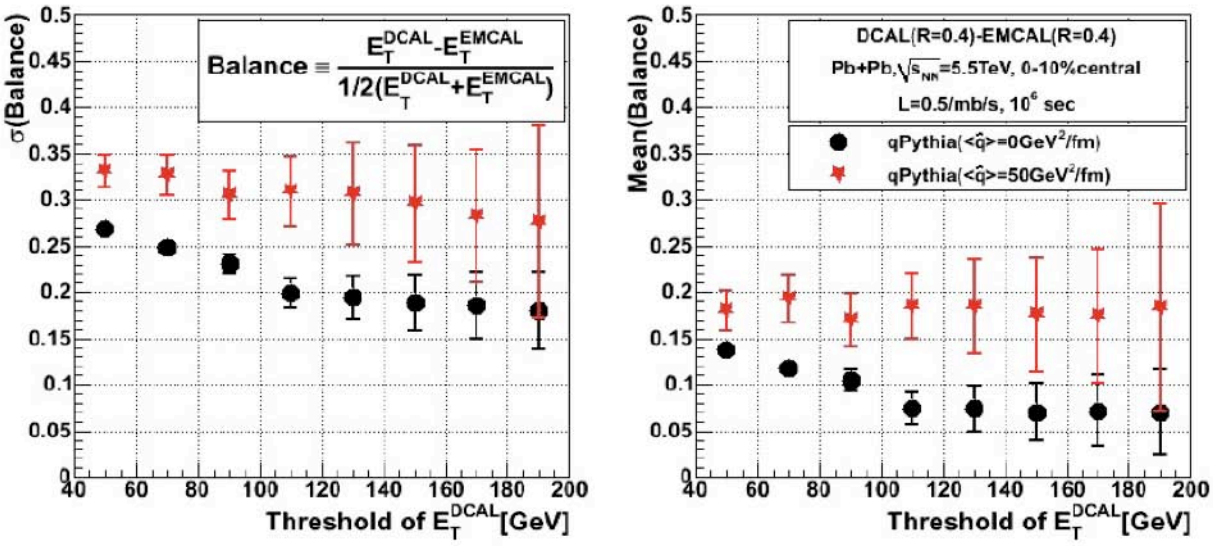

Figure II.8 Threshold dependence of Gaussian fit parameters from Figure II.7.

It should be noted that these calculations have not included the effects of the incoherent heavy ion background in central Pb+Pb collisions, which is beyond the scope of the present study. The effect of such backgrounds will be to enhance the tails seen in Figure II.7 in the region of $\Delta \sim 2$, with smaller effects for larger threshold in the DCal. Correction for such backgrounds will require an unfolding procedure that is similar in nature, though different in detail, to that applied to inclusive spectra. However, it should be noted that the physics bias induced on the semi-inclusive recoil jet spectrum by the trigger jet requirement corresponds to a strong suppression of low energy recoil jets, resulting effectively in a harder jet spectrum than the unbiased population. As has been shown by heavy ion jet analysis in STAR (M. Ploskon (STAR Collaboration), 2009), the spectrum distortion due to underlying event non-uniformities is much smaller for a semi-inclusive spectrum that is biased (i.e. hardened) in this way, and it can therefore be measured with greater systematic precision than the inclusive jet spectrum.

We make no attempt here to estimate the precision with which such a correction can be made, though experience with inclusive spectra (ALICE EMCal Physics Performance Report, 2009; M. Ploskon (STAR Collaboration) 2009) shows that effects of heavy ion background can indeed be brought under quite precise quantitative control. Our aim here is to demonstrate the potential signal and statistical reach of such an observable; full investigation of corrections to such a measurement is a longer term project.

II.3.4.2 Path-length bias: π^0 + jet measurements

It is well established that high p_T inclusive hadron production in nuclear collisions is highly biased due to jet quenching. Model studies show that the combined effect of large energy loss and the steeply falling production spectrum cause the observed hadron yield at a given p_T to be dominated by fragments of jets that did *not* interact in the medium, in particular jets generated on the surface of the fireball and initially headed outwards.

Triggering on a high p_T hadron (π^0 in the DCal) provides a unique bias of the jet population recoiling azimuthally opposite to the trigger: due to jet quenching, the hadron trigger arises dominantly from jets generated at the surface and headed outwards, thereby *maximizing* the path length of the recoiling jet in matter. The measurement is semi-inclusive: given a π^0 trigger, what is the distribution of recoiling jets? Figure II.9 is a simplified diagram of the geometry, showing the projection of the interaction fireball on the transverse plane with the trigger pion traveling to the right, traversing length *L1* in matter, while its recoil travels length *L2* in the opposite direction.

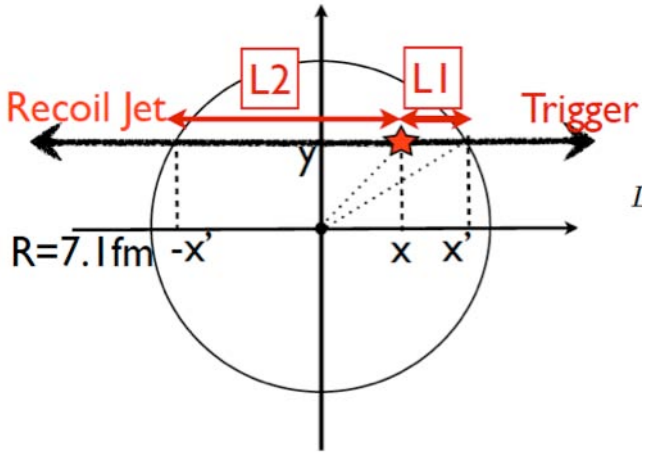

Figure II.9 Geometry of trigger and recoil in hadron+jet production

The geometric bias induced by a hard pion trigger is shown in Figure II.10, calculated using qPYTHIA for various thresholds of π^0 p_T and various values of qhat. The figure shows the position of hard scattering in the transverse plane, for interactions generating a π^0 with p_T above a given threshold and moving to the right. For qhat = 0 (top row), the distribution follows the unbiased distribution of hard scatterings, whereas for larger qhat (bottom two rows) and high π^0 E_T (right column) the distribution is strongly biased towards short path length for the jet that generates the π^0 trigger.

There is little difference in the bias between qhat =20 and 50 GeV^2/fm, indicating a largely opaque core of the fireball in both cases. This suggests that the geometric path length bias can be calculated reliably, without strong dependence on the details of the quenching. A more significant difference is observed for trigger conditions $E_T > 5$ GeV and $E_T > 20$ GeV,

with the latter case exhibiting much stronger bias. This suggests (within the qPYTHIA model) that pion production at ~5 GeV/c may not be strongly biased towards leading jet fragments. Measurements with a large dynamic range in pion threshold are therefore needed, and can only be provided in an efficient way by a fast (Level 1) trigger in the DCal.

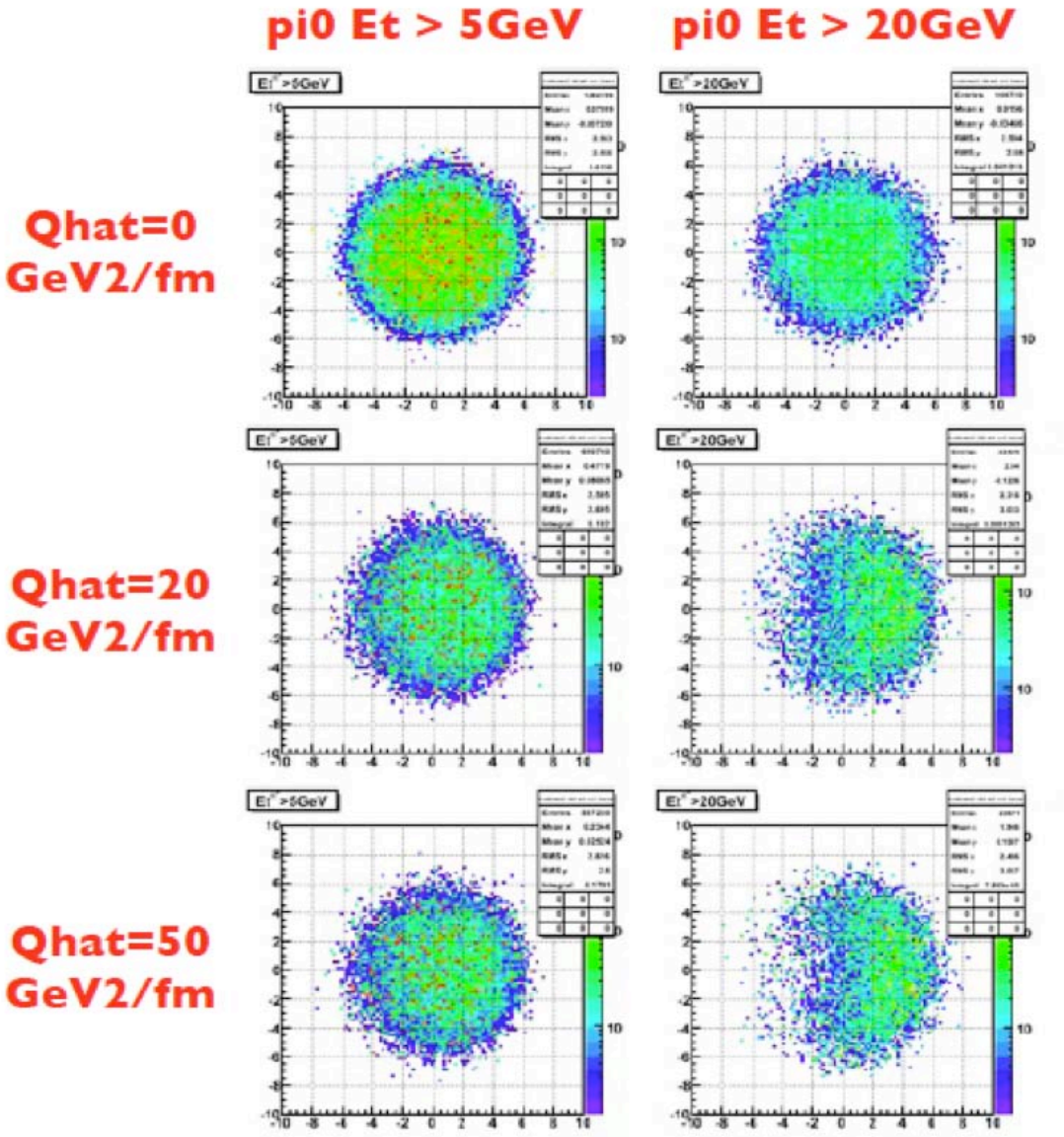

Figure II.10 Distribution in transverse plane of hard scattering vertices that generate a hard pion moving to the right, for various qhat and pion trigger E_T thresholds.

The path length bias for both the trigger jet (generating the pion trigger) and the recoil jet are shown in Figure II.11, for various qhat and pion trigger thresholds. The reference distribution (qhat=0) is shown by the black circles. A marked bias of several fm is seen for both jets. As discussed in section II.2 on RHIC measurements, triggering on a high p_T

hadron (π^0 in the DCal) provides a bias of the jet population recoiling azimuthally opposite to the trigger: due to jet quenching, the hadron trigger arises dominantly from jets generated at the surface and headed outwards, thereby *maximizing* the path length of the recoiling jet in matter.

The path length biases in Figure II.11 exhibit little dependence on qhat and pion trigger threshold as long as these parameters are large enough. This lack of sensitivity of the bias to the dynamics suggests that the geometric bias can be calculated reliably, without strong dependence on the details of the calculation.

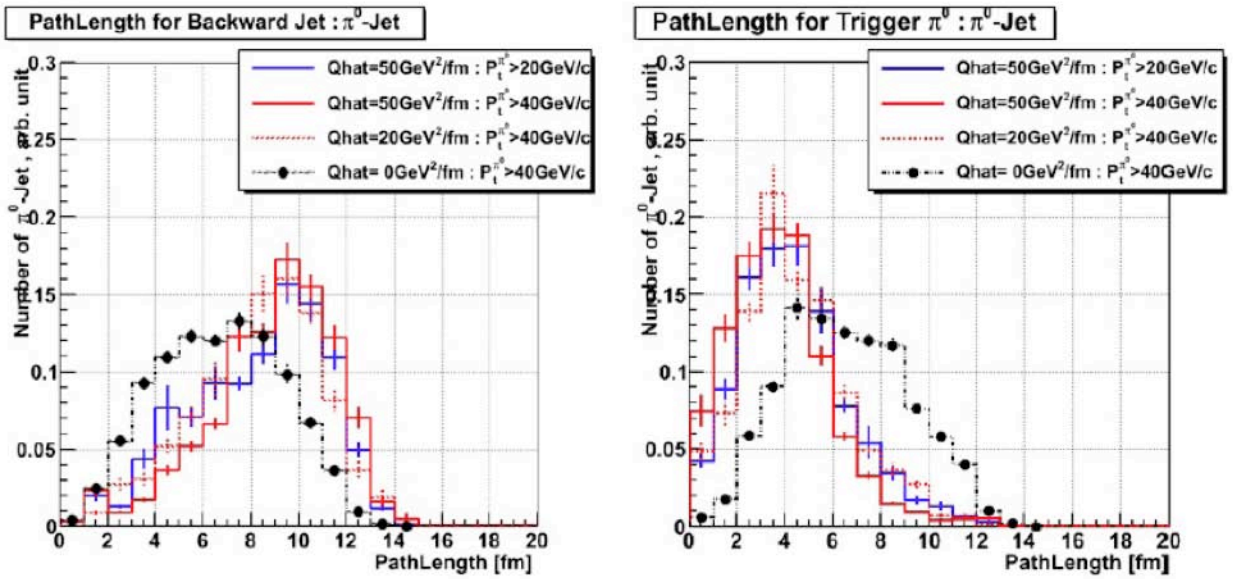

Figure II.11 qPYTHIA calculation of path length distributions for a semi-inclusive π^0+jet measurement in central Pb+Pb collisions. The path length distribution of the trigger pion (right) and otherwise-unbiased recoil jet (left) are shown for various qhat and pion trigger thresholds. The reference distribution distribution without quenching (qhat=0) is shown by the black circles.

Figure II.12 shows the expected annual yield of jets in the EMCal acceptance (specifically, the number of jets above a given energy threshold, per heavy ion running year) recoiling from a π^0 trigger in the DCal with $E_T > 20$ or 40 GeV, for various values of qhat. Since the trigger is a π^0 and not a jet or prompt photon there is no significant kinematic constraint on the energy of the recoil jet, which at very high jet E_T parallels the unbiased distribution, but at reduced rate due to the requirement of a hard pion trigger in the event.

The strength of the quenching influences not only the broadening and softening of the fragmentation of the recoiling jet in the EMCal, but also the rate of high E_T π^0 triggers in the DCal. For a π^0 threshold of 20 GeV, the recoil jet spectrum in the EMCal has 1000 counts above 90 GeV for one heavy ion running year of Pb+Pb collisions. Comparison to the inclusive (unbiased) jet population in the EMCal, also shown in the figure, shows a

reduction in jet rate in the EMCal of a factor 10-50 at high E_T, relative to the unbiased population for this configuration.

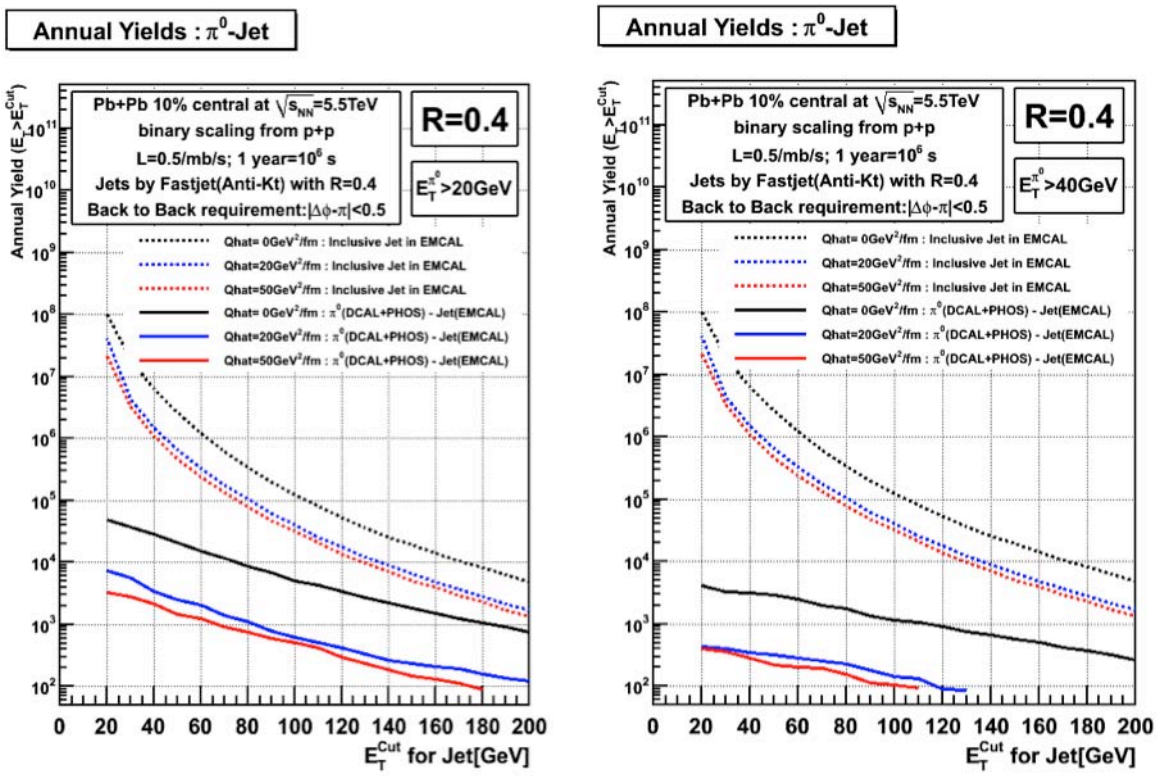

Figure II.12 Annual yields for π^0+jet correlation measurements for various values of quenching parameter qhat, with the π^0 triggered in the DCal above a threshold of p_T = 20 GeV (left) and 40 GeV (right).

Figures II.13 and II.14 show the primary observable of interest, the semi-inclusive spectrum of jets (anti-kT, R = 0.4) measured in the EMCal, recoiling azimuthally back-to-back from a π^0 trigger in the DCal with threshold 20 or 40 GeV/c, with path length bias indicated in Figure II.10**.** The distributions are normalized per trigger, and are shown for qhat = 0, 20 and 50 GeV^2/fm. The error bars show the statistical error expected for one year of running with Pb+Pb at 5.5 TeV and nominal luminosity, corresponding to 0.5 nb^{-1}. The ratios of the spectra for finite qhat to that for qhat = 0 are shown in Figure II.14.

A strong, and qhat-dependent, suppression in the recoil jet yield is seen in both figures. Sufficient statistical precision is achievable in one running year to discriminate the simulated quenching scenarios well, for recoil jet energies above 200 GeV. This is a unique measurement, with very broad kinematic reach. It will complement the inclusive jet R_{AA} measurement reported in the EMCal PPR (ALICE EMCal Physics Performance Report, 2009) in much the same way that R_{AA} and I_{AA} for high p_T hadrons complement each other at RHIC. We expect measurements of hadron+jet correlations, together with related observables measuring the detailed topology of the recoiling jet, to provide very strong

constraints on the theoretical description of jet quenching. The DCal, including its fast triggering capabilities, is essential for this measurement.

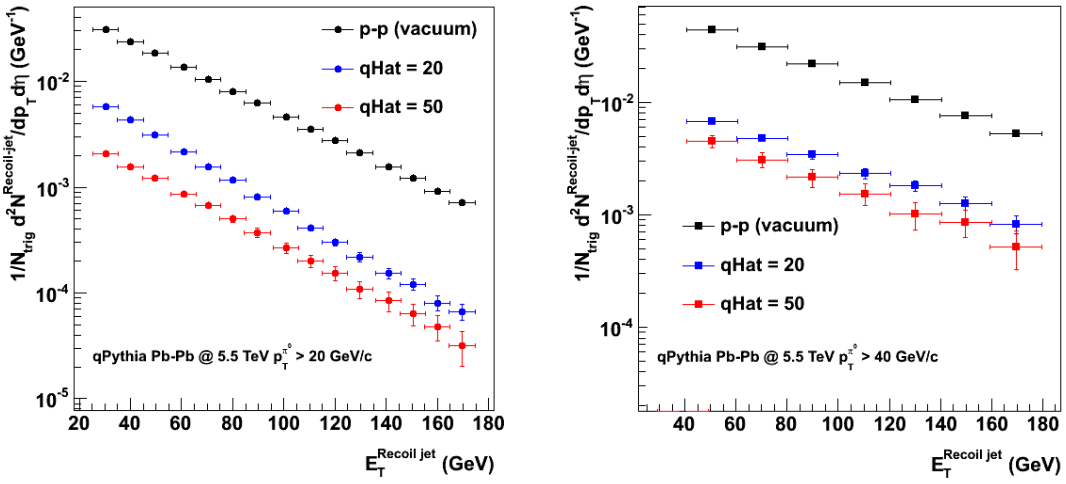

Figure II.13 Semi-inclusive jet spectrum measured in EMCal (anti-kT, R = 0.4), recoiling from a π^0 trigger in DCal above p_T thresholds of 20 GeV/c (left) and 40 GeV/c (right), for various qhat. Error bars show statistical errors expected for one year of running for Pb+Pb at 5.5 TeV (0.5 nb^{-1}).

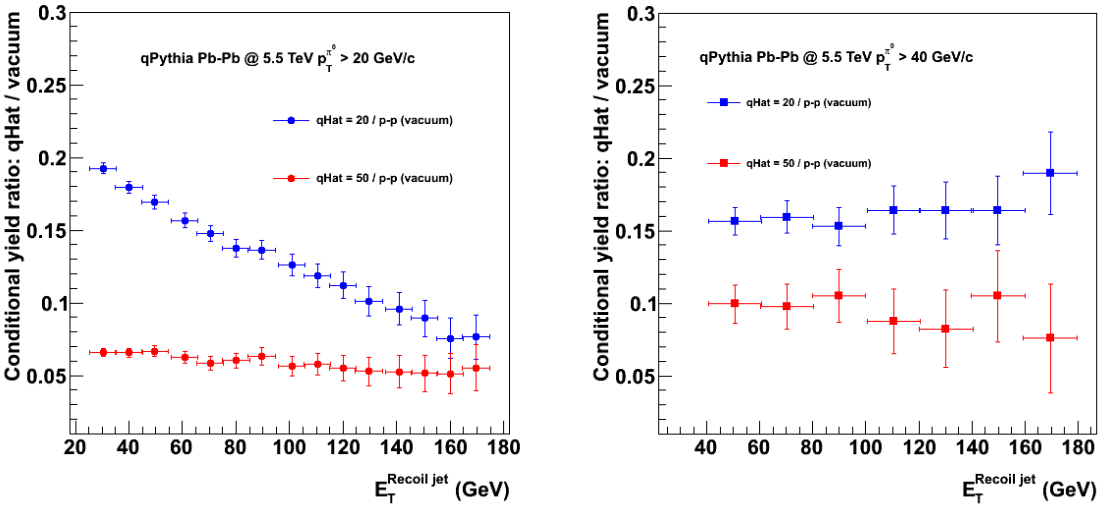

Figure II.14 Ratio of semi-inclusive jet spectra in Fig II.13 in the EMCal recoiling from a π^0 trigger in the DCal above p_T thresholds of 20 GeV/c (left) and 40 GeV/c (right), for qhat = 20 (blue) and 50 (red) relative to spectrum for qhat = 0. This corresponds to I_{AA} measured for di-hadrons. Error bars show statistical errors expected for one year of running for Pb+Pb at 5.5 TeV (0.5 nb^{-1}).

Bibliography

Abelev, B. I. et al. (STAR Collaboration) 2006, *Phys. Rev. Lett. , 97*, p. 252001.
Adams, J. et al. (STAR Collaboration) 2003, *Phys.Rev.Lett , 91*, p. 072304.
Adams, J., et al. (STAR Collaboration) 2006, *Phys. Rev. Lett. , 97*, p. 162301.
ALICE EMCal Physics Performance Report, 2009, from http://rhic.physics.wayne.edu/~bellwied/ppr/ppr-final-nov13.pdf.
E. Bruna (STAR Collaboration) 2009, "Measurements of jet structure and fragmentation from full jet reconstruction in heavy ion collisions at RHIC" *Nucl. Phys. A830*, 267C (2009).
M. Ploskon (STAR Collaboration) 2009, "Inclusive cross section and correlations of fully reconstructed jets in $\sqrt{s_{NN}}$ = 200 GeV Au+Au and p+p collisions" *Nucl. Phys. A830*, 255C (2009).
N. Armesto, L. C., 2009, "Q-PYTHIA: A Medium-modified implementation of final state radiation" *Eur. Phys. J. C63*, 679 (2009).
Putschke, J. et al. (STAR Collaboration), 2009, *Eur.Phys.J. C61*, p. 629 (2009).
Salur, S. et al. (STAR Collaboration) 2009, *Eur.Phys.J. C61*, p. 761 (2009).

III. DCal Functional Requirements and Detector Overview

We start the discussion of the DCal detector with its physics-driven functional requirements. The ALICE DCal project must deliver an electromagnetic calorimeter with acceptance sufficient[3] for di-jet reconstruction in central Pb+Pb collisions and an energy resolution and an electromagnetic shower shape determination sufficient for π^0/γ discrimination up to at least $p_T \sim 30$ GeV/c in central Pb-Pb collisions. These are the critical considerations that the detector design must meet for the ALICE-DCal physics program. The primary detector design goal is to meet these latter specifications at the lowest possible cost and on a schedule optimized to match the LHC running and shutdown planning. The functional requirements for the DCal can be scaled directly from the ALICE EMCal Requirements[4]. The system parameters desired for the ALICE DCal are as follows:

1. Large effective acceptance for di-jets when used with the EMCal with analysis cones up to radii R = 0.4. This is satisfied by a detector spanning 60 degrees in azimuth and 1.4 units of pseudo rapidity placed back-to-back with the corresponding 60 degrees in azimuth of the ALICE EMCal.
2. A photon or electron energy resolution better than or equal to $\sigma(E)/E =$ [redacted] $\oplus$ 3% averaged over the full detector acceptance at energies above 2 GeV and less than 100 GeV. At this resolution, the ALICE DCal energy measurement for electrons is comparable to the ALICE tracking system momentum measurement for $p_T > 20$ GeV/c.
3. A detector granularity and analog noise sufficient for π^0/γ discrimination in central Pb+Pb collisions out to transverse momenta of at least ~30 GeV/c. This requires greater than a factor of 2 suppression of the π^0 background at this transverse momentum based on shower shape.

These requirements lead us to adopt a basic detector design identical to that employed in the ALICE EMCal. In the following discussion, we will present a detector that uses the same module design and the same integration of modules into strip units (strip modules) and then the assembly of these strip units into super modules. Super modules are the units handled at installation into ALICE. Indeed, the DCal is in every way and extension of the EMCal acceptance into a new phi range with the exception that allowance must be made for the space occupied by the existing PHOS detector.

[3] i.e., an acceptance sufficient to provide adequate statistics to permit energy balance measurements for di-jets with p_T up to ~150 GeV/c.

[4] The EMCal Physics Performance Report, EMCal_ppr.pdf, can be found at http://rhic23.physics.wayne.edu/~cormier/.

IV. Project Management and Overview

The ALICE DCal is a joint Chinese /Finnish/French/Italian/Japanese/Swiss/U.S. project. Back-to-back with the EMCal, the ALICE Experiment can accommodate up to a total of 6 detector units[5] or DCal "super modules". The responsibility for the production of these super modules and/or associated components is described in section VII.

The full International DCal Project is being managed within ALICE in a manner identical to the management structure used for the EMCal. A management board (DCal-MB) has been created with representation from all national groups. This Board is responsible for the overall coordination of the different national efforts contributing to the project to insure the most efficient utilization of resources, monitor technical matters bearing on design, fabrication and quality control and to nurture the development of the combined EMCal / DCal scientific program within ALICE. The U.S. Project Manager, T.M. Cormier (Wayne Sate University and LBNL), chairs the DCal-MB and serves as DCal project leader within ALICE. C. Roy (Strasbourg) and N. Bianchi (Frascati) serve as deputy project leaders. J. Rasson (LBNL) serves as Technical Coordinator for the full International DCal Project.

In the execution of its responsibility to ensure the success and productivity of the international DCal project, the MB has coordinated, largely taken over from the EMCal project, the development of a single DCal final design, a single set of assembly tools and procedures, a single set of QA/QC protocols and a single test, calibration and commissioning procedure. This is done to ensure that the DCal will function as a single detector within ALICE and quickly achieve the common scientific goals of all the national groups.

Within the overarching coordinating structure provided by the DCal-MB, each of the national projects retains full responsibility for its own deliverables. These responsibilities are formalized in a single *"Letter of Intent to Collaborate"* (LOI) document signed by all of the national groups. This document is the basis for tracking expected contributions and deliverables to the final DCal scope from various national groups.

[5] This notation indicates 6 full size super modules and associated readout electronics.

V. R&D and Operational Experience with the DCal Design

A substantial program R&D carried out for the EMCal project supports the design and production procedures chosen for DCal. A program of EMCal R&D was completed prior to approval of the EMCal project. The objective of the EMCal R&D was to explore detector technology options and study detector performance for these technology alternatives. Prior to EMCal funding approval, an approximately 0.5m x 0.5m prototype was operated in a test beam at Fermi National Accelerator Laboratory (FNAL) to explore operational features of the preferred mechanical/optical technology. The results of the test strongly supported the basic conceptual design and only minor revisions in the mechanical and optical design were necessary. During the first full year of the EMCal funding, R&D efforts continued with the completion of another small prototype built from modules of the final-design followed by a second test beam experiment performed on the CERN PS and SPS accelerators. The goal of this second test beam was to establish the operational characteristics of these final-design modules, so that further progress could be made on software and simulation effort, and to demonstrate integration with ALICE online and data acquisition (DAQ) in a full systems test under realistic conditions with beam. Finally, 4 full size EMCal super modules have operated successfully as part of ALICE in LHC runs in 2009 and 2010. These various steps in the test and implementation of the EMCal precede the DCal project and now supply an important base from which to predict DCal operational characteristics as well as for the verification of material, components and labor cost estimates that define the cost and schedule baseline of the DCal project.

VI. Detector Design

In the following sections, the major aspects of the detector design are summarized.

VI.1 Detector Modules and Super Modules Design and Fabrication

The full acceptance of the DCal electromagnetic calorimeter consists of a barrel section providing coverage for a 60^o arc in azimuth and 1.4 units of pseudo rapidity along the beam direction. Figure VI.1 shows the beam view of EMCal and DCal. Three 20 degree ϕ-segments of EMCal are back-to-back with three 20 degree ϕ-segments of DCal. This is the maximum back-to-back coverage possible in ALICE given the installed location of the EMCal and the ALICE space frame support system.

Each 20 degree ϕ-segment of EMCal comprises two EMCal super modules each spanning $\Delta\eta$=0.7 units of pseudo rapidity. The resulting full EMCal coverage for a total of 10 super modules is $\Delta\eta$=1.4 x $\Delta\phi=100^o$. The corresponding full coverage for DCal is $\Delta\eta$=1.4 x $\Delta\phi=60^o$ but is built up from effectively 6 separate DCal "super modules" and 3 PHOS modules spanning in combination the full acceptance. This is illustrated in figure VI.2 which shows the 6 DCal super modules and a total of 4 PHOS Modules – only three of which are contiguous with DCal super modules. At the moment, only these 3 PHOS super modules are installed in ALICE and the other one is pending funding. In any event, the single missing PHOS module is not relevant to the proposed DCal physics program.

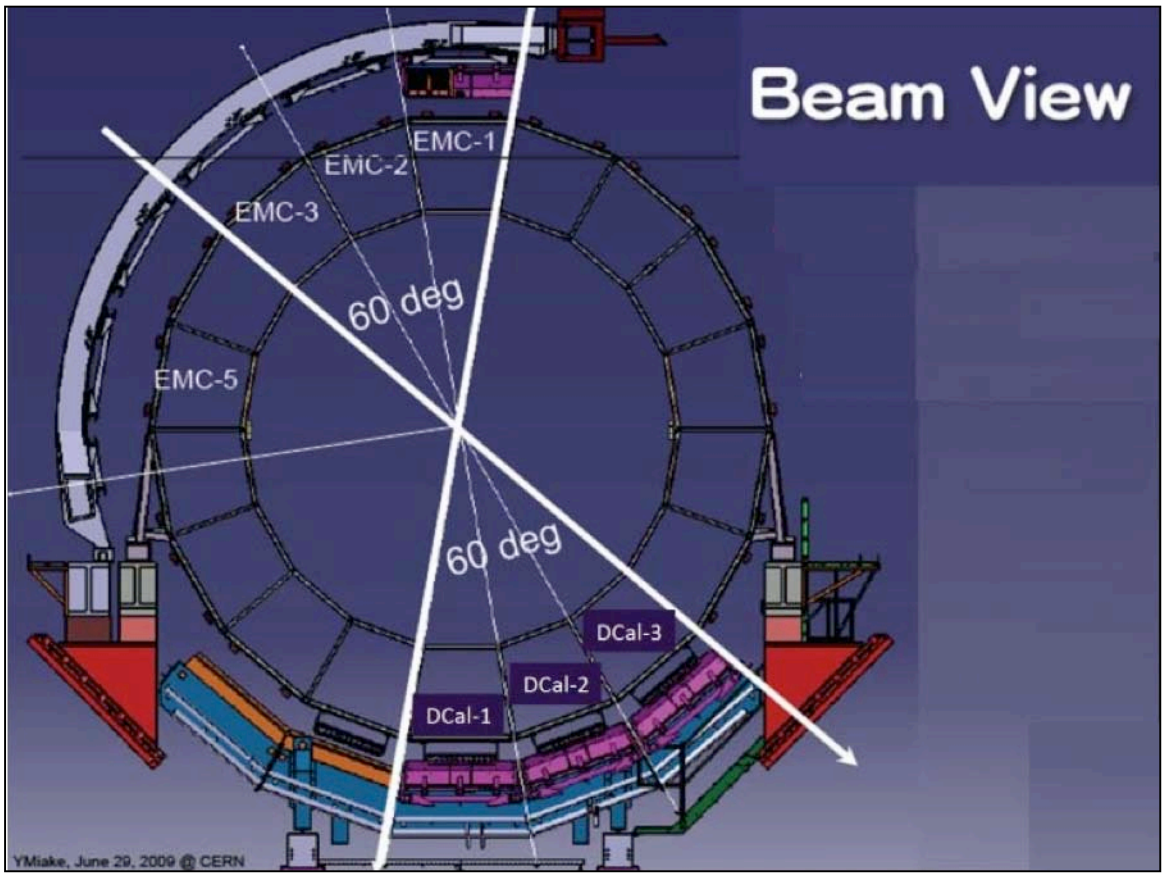

VI.1 Beam view of EMCal (above mid-plane) and DCal (below mid plane).

PHOS is a high-resolution, highly segmented, electromagnetic calorimeter based on $PbWO_4$ crystals. It shares with the EMCal and DCal common readout and trigger electronics. Like the DCal super modules, each PHOS module subtends $\Delta\phi$=20 degrees. The presence of the PHOS detector at the center of the DCal acceptance shortens the DCal super module to exactly 2/3 the length of the standard EMCal super module. This is illustrated in Figure VI.3 where an EMCal super module is compared to a DCal super module.

The use of two different detector technologies in the assembly of DCal creates some extra "cracks" in the acceptance compared to EMCal. These cracks between PHOS and DCal super modules are very small compared to the area of a jet of R=0.4 and detailed simulations verify that they have negligible impact on di-jet or inclusive jet measurements with DCal (see chapter II). In the case of inclusive π^0or π^0- triggered hadron correlation measurements the presence of the extra crack requires a small additional fiducial cut which slightly reduces the total acceptance. The π^0 or π^0- associated hadron yields are so large, however, that the additional fiducial cut has no impact on physics.

DCal super modules are built up exactly as they are in EMCal, out of strip modules with each strip containing 12 modules of 4 towers each. All of these building blocks including

all readout and trigger electronics are identical and interchangeable between EMCal and DCal. The details of the module and strip module construction, optical read out, electronics and cosmic ray calibration are explained in detail in the EMCal Technical Design Report (CERN-LHCC-2008-014, ALICE-TDR-014, 1 September 2008) and will not be repeated here.

As noted above, because of the presence of the PHOS modules centered at zero rapidity, the DCal super modules are shorter such that the full DCal will subtend the same overall rapidity coverage as EMCal. Figure VI.3 shows a comparison of DCal and EMCal super modules. The construction is identical except that the full DCal super module will contain only 16 strip modules compared to 24 in EMCal.

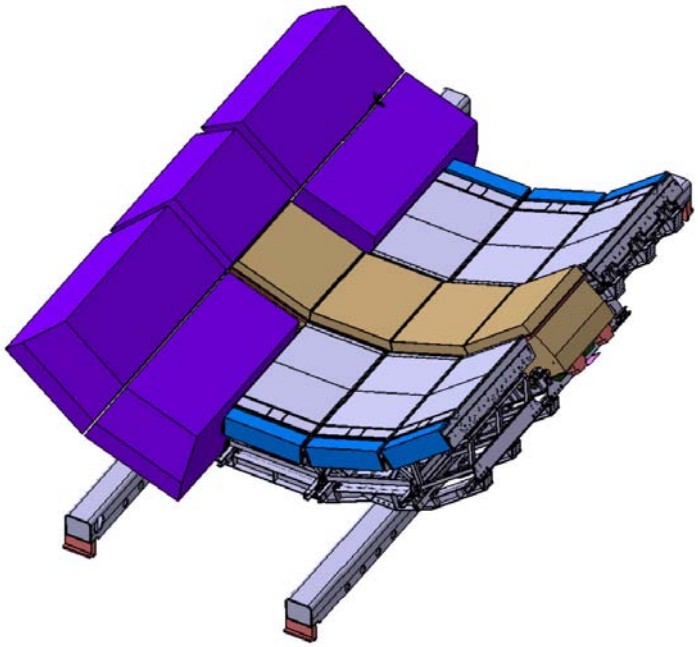

VI.2 Perspective view of the DCal and PHOS integrated on a common support. The PHOS charged particle veto detectors are in place in front of the PHOS modules. As discussed in the text, the support structure is a component of the full international project scope. Four PHOS modules are shown although only three, those contiguous with the DCal, are installed in ALICE at the moment and considered part of DCal. Also shown on the support structure, to the left of DCal, are five super modules of a hypothetical Very High Momentum Particle Detector (VHMPID) which is currently under discussion in ALICE.

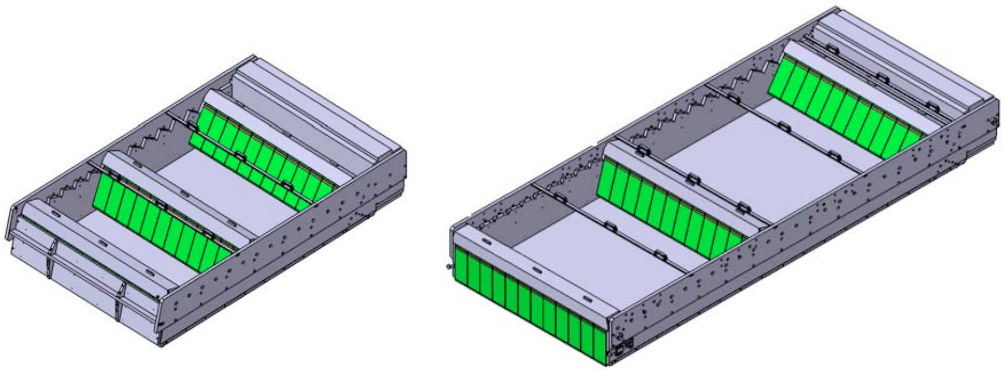

VI.3 A comparison of a DCal (left) and EMCal (right) super modules. In each case only 3 strip modules are indicated for clarity. Modules and strip modules used in EMCal and DCal are identical. Only 16 strip modules per DCal super module are used compared to 24 for the EMCal super module.

VI.2 Detector Support Structure Overview

A new support cradle to accommodate both PHOS and DCal are part of the scope of this project. In addition, to accommodate the heavier combined weight of PHOS plus DCAL, new "PHOS" rails are required for the full support structure plus the DCal and PHOS detector weight. The following requirements were developed for the full support structure – rails plus cradle - in collaboration with ALICE Technical Coordination.

Table VI.1 Requirements for support structure

1. DCal and PHOS detectors have to be inserted and removed in same way as EMCal super modules, by sliding one by one on rails parallel to beam axis and mounted on the support cradle.
2. Support structure should allow full accessibility to PHOS modules for maintenance.
3. Support structure should not interfere with emergency operations particularly for personnel
4. Support structure should give enough clearance for all ALICE services
5. Support structure should allow access to stairways on ALICE A and C sides.
6. Support structure should be fully assembled within ALICE without disturbing the mini frame
7. Insertion of detectors should be achieved without dismounting mini frame
8. The system should not induce any modification of the PHOS detector

One end of the L3 magnet is permanently closed to access because of the muon arm absorber and dipole magnet. Therefore the insertion of the new "PHOS" rails and all structures associated with the support cradle and all detector super modules must take place via the ALICE A-Side. Figure VI.4 shows the ALICE A-Side with the mini space frame in place and the L3 doors open. This is the configuration that will be available during DCal support installation and detector installation. The final design[6] that has been realized in collaboration with ALICE Technical Coordination and in consultation with PHOS has met all the requirements listed in Table VI.1. In the following sections, we discuss the main design, fabrication and integration tasks associated with implementing DCal in ALICE.

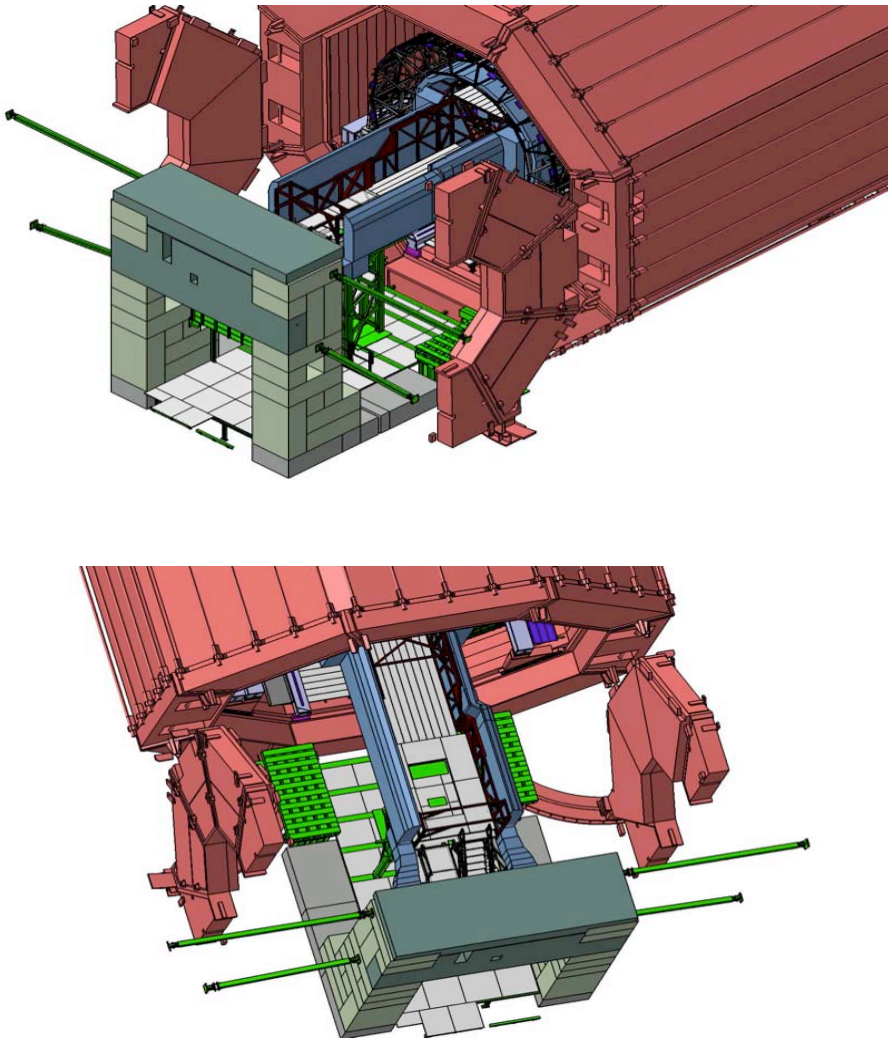

Figure VI.4 A-Side of the L3 magnet with the doors open and the mini space frame in place. All installation activity associated with DCal – rails, support cradle, PHOS modules and DCal super modules - must take place without disturbing the mini space frame

[6] An external final design review was organized by ALICE and completed on May 25, 2010

VI.3 New "DCal" Rails

Two beams (previously so called "PHOS" rails), parallel to Z axis and directly linked to L3 at the A-side and C- side are used to support the full load of DCal and PHOS. One rail is on I side, the other one on O side. The clearance between the 2 rails is 3710 mm. The original PHOS rails were designed to support only 5 PHOS modules. We now need to support a substantial additional load as specified in Table VI.2

Table VI.2 Component weights to be supported by the new "PHOS rails

1. DCal, 6 Super Modules, 5t each
2. 4 PHOS modules, 5t each
3. 5 VHMPID modules, estimated 1t each
4. 4 CPV modules, 0.15t each

Total load on 2 rails will be 70t, with a 45.6t max load on I side rail, and 23.7 t load on O side rail.

In order to meet ALICE requirements for non-magnetic materials the new rails will be fabricated from 1.4311 austenitic stainless steel (304LN). This material has a yield strength ($R_{p0.2}$) of 270 MPa, (allowed stress 245 MPa see below) and an ultimate tensile strength 550 MPa. To preserve the overall non-magnetic character of the support beams, the amount of ferrite in welds will be held to within 5 to 8 %.

The final fabricated rails will have a length of 12235 mm to span the entire length of the L3 magnet and utilize existing interfaces. The beam width is 500 mm with the upper face located at Y=-5310 mm from the beam axis. The vertical height of the beam is chosen to maintain a minimum of 140 mm clearance to the L3 floor to provide space for existing and potentially new services.

Unlike the original PHOS rails that are I shaped, the new DCal rails will be rectangular tubes in order to avoid any lateral-torsional buckling that could occur on the vertical web of an I shaped beam. For a given weight and a given flexure load, a tube beam also performs at lower maximum stress than an I-beam. As a side benefit, the tube rails can also be used as ventilation ducts for cooling air inside L3. This will allow a substantially better distribution of cooling air than the previous ventilation system which has only one central air duct with a few outlets. The previous ventilation system was also not well located for accessibility to PHOS and to cradles.

The DCal tube beam, is a custom fabrication to be made from welded parts. Traditionally, a rectangular tube should be made from 4 welded side plates. The disadvantage of this option is that welds are located in high stress areas for a flexure loading. With the 4 welded sides option, the only one way to decrease the stress in welds down to allowable (safety code) values, is to increase size and stiffness of the beam. This leads to substantially higher costs and results in limited clearance for surrounding services and equipment.

A horizontal beam with a flexure loading has maximum stress on its upper face (compression) and lower face (traction). The medium plane (neutral plane) has stress close to zero. An optimized design, therefore, should locate welds and any large holes, etc., in these areas. For this reason, the tube beam is welded in the medium plane.

This design option requires a raw plate to be folded into a U shape and welded over 12 m in length with high tolerances on straightness (± 5 mm) as indicated in figure VI.5.

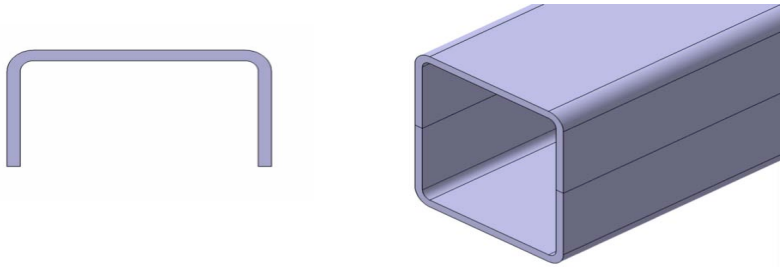

Figure VI.5 Rectangular tube beam structure to be used for DCal and PHOS

VI.3.1 Finite Element Calculations

VI.3.1.1 Deflections

FEA calculations were done with 2 different FEA applications: SAMCEF and ANSYS.
The loading used in the FE calculations was 1.35 times real loading, according to standard ENV 1993-1-1, Eurocode-3. A second safety factor is applied on Yield Strength of the material which is degraded by a factor 1.1. That means that the allowed strength is 270 / 1.1 = 245 MPa.

Figure VI.6 shows the distribution of weight on the O-Side and I-Side beams. At full loading the Center of Gravity (CoG) of the assembly is located 663 mm to the right of the median plane. One can see, that during insertion process, the sequence of events should be chosen to keep the CoG as close as possible to the median plane in order to avoid any overstress on the I-side rail.

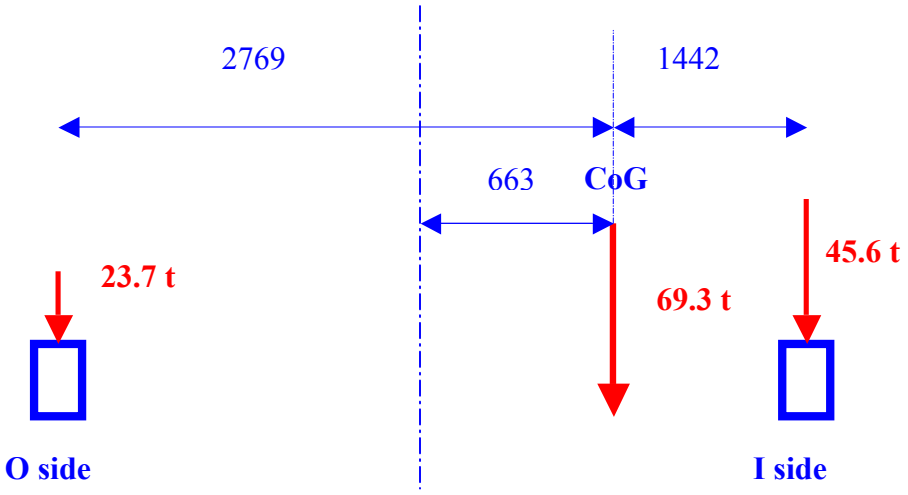

Figure VI.6 Sharing of load between O rail and I rail, versus location of CoG

Under the loading shown in figure VI.6 the maximum deflection of I-Rail is 32 mm while the deflection at rib #1 of the support cradle (see section VI.4) on the A side, is 21 mm. Similarly, for a 23.7t load, the maximum deflection of O-Rail is 18 mm while the deflection at rib 1 on the A side, is 12 mm. The deflection of rail under its own weight is 2.2 mm.

VI.3.1.2 Stress Calculations

Our stress results are presented as mean Von Mises equivalent stress, by finite element. The mean value is computed, in an element, by summing the values attached to its nodes and the dividing by its number of nodes. As expected, the stress is maximum in central areas, and minimum at support area, with the medium plane at nul stress which results from the inversion of stress from compression to tension. The results are shown in figure VI.7.

The holes for ventilation are seen in figure VI.7 along the median plane of the beam. Holes for ventilation do not affect significantly stresses, when they are centered on neutral plane, and when their diameter does not exceed 100 mm.

The 2 rails are designed to have a capacity that allows for future upgrades. The present design allows a total load on each rail not to exceed 50t during insertion process and after full integration.

After the final design review of the support structure, some inner stiffeners are now foreseen, located where the load is applied on rails, in order to decrease stress and increase margin with possible stability problems.

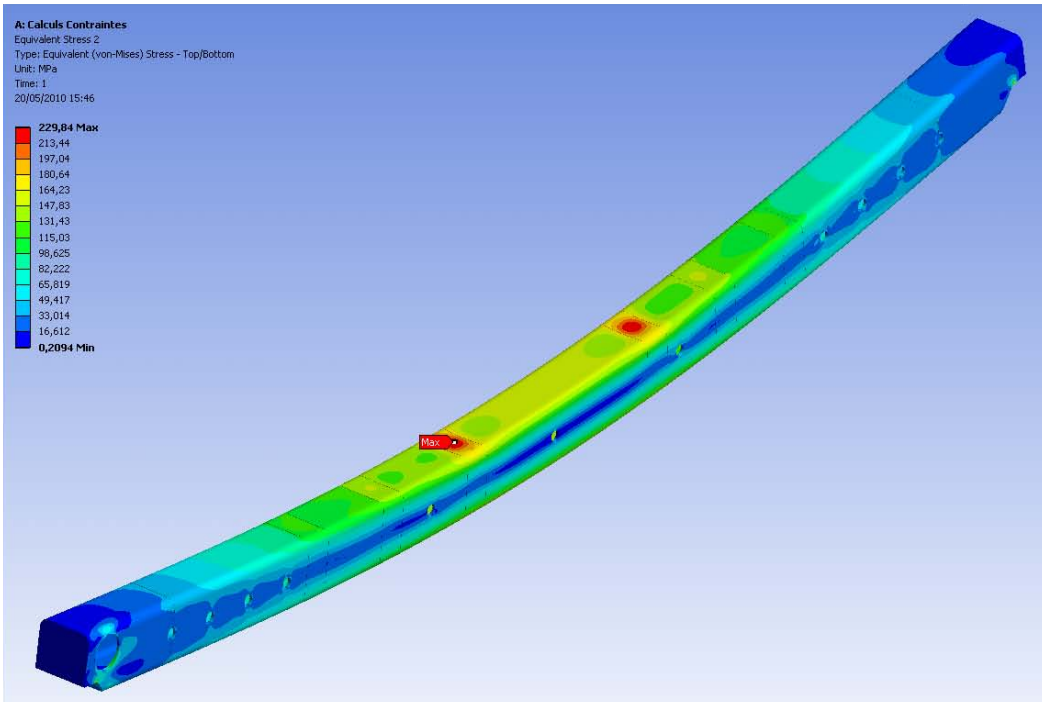

Figure VI.7 An overview drawing of the FEA results for stress in one beam loaded to 45.6t. The maximum stress points occur at the location of support cradle ribs number 3 and 4. The maximum stress is 207 MPa.

VI.4 DCal - PHOS cradles

A cradle system is mounted on the new "PHOS" rails to enable the support and accurate positioning of both the PHOS modules and the DCal super modules. The cradle functions as an integral component of the installation system. In addition to the general requirements for the complete support structure given in Table VI.1, the cradle must satisfy the additional, specific, requirements listed in Table VI.3.

Table VI.3 Requirements for Cradles

1. Non magnetic raw material and components
2. Must allow full accessibility to PHOS for maintenance
3. Must allow insertion and removal of detectors one by one: removal of one PHOS module, for example, should not require to removal of all A side DCal super modules or the removal of all PHOS modules (which is the present situation).
4. System design should minimize dead area between DCal and PHOS.
5. The cradle should exhibit minimum deflection under full load with maximum stress in rib members < 245 MPa
6. Total weight of any component should be minimized to permit for easy handling inside L3
7. System should be compatible with other extensions and upgrades

VI.4.1 Conceptual design of cradles

The cradle system is illustrated in figure VI.8. There are 2 actually separate cradles - one on the A-side and one on the C-side. Because there is no crane or heavy lifting facilities inside L3, it is not possible to insert a fully assembled cradle into L3. Furthermore, the available room in front of the L3 magnet, given the mini frame is in place and may not be moved is quite restricted with very limited crane access. Figure VI.4 shows the area adjacent to the mini frame and outside the L3 magnet where crane coverage within the L3 hall is still possible. Into this space, beam-like components of the cradle no larger than 3000 mm in length may be lifted and rigged into the L3 magnet using specialized tooling. These components are then assembled, bolted and pinned, in place inside L3. Each cradles are composed primarily of 3 ribs which, after assembly, are bolted and clamped to the rails to complete the cradle.

Extruded aluminium rails, parallel to beam axis, are bolted on the ribs and will support DCal super modules and PHOS modules. These aluminium rails are identical to the rails used in the EMCal to fix the super modules to the Cal-Frame and to allow the translational motion of the super modules in the z-direction from inside the insertion tool, located outside the L3 magnet, to their final resting place during installation. The EMCal TDR should be consulted for details concerning the function of the extruded aluminium rails. Rails (both the large ones and the small aluminium ones) may be considered part of the mechanical structure of the cradles, as they rigidly link the ribs together.

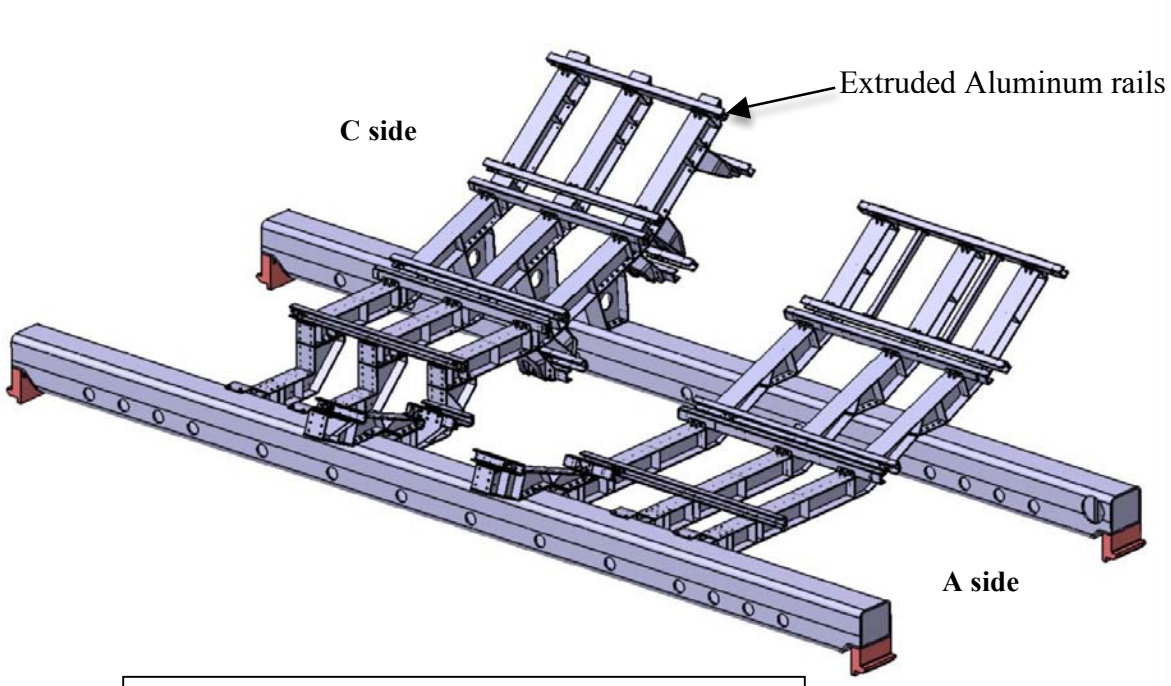

Figure VI.8 The DCal and PHOS support cradle

VI.4.2 Description of DCAL-PHOS-VHMPID cradles

The ribs will be made from welded plates, of 1.4311 stainless steel, 10 and 15 mm thick.
The cross section of ribs will be I shape. Each rib on the A-side is approximately 700 kg in weight. The complete cradle on the A-side weighs roughly 3500 kg. Each rib on the C-side has a weight of approximately 900 kg and the complete cradle C-side weighs roughly 3900 kg.
Each rib will be commercially inspected by APAVE institute or equivalent, before shipping to ALICE.

The individual ribs will mounted on the "PHOS" rails, one by one, moved into position with custom rigging tooling, starting with C-side ribs. Fixation of ribs to rails is done with M20 bolts. All bolts and screws used in cradles are austenitic stainless steel.

After fixation of the ribs on the large rails, the U shaped, extruded aluminium rails will be mounted on ribs. The aluminium rails are not at the same height on A-side and C-side. This is clear in figure VI.8 and VI.9. On the C-side the rails have mainly to support 373 mm thick DCal super modules. The detector elements of the DCal super module have a rather high density, low sampling fraction, design which makes them very compact. Twenty radiation lengths of active detector plus its photo sensor and pre amp are all contained in this 373 mm thickness.

On A side, however, the extruded aluminium rails have to allow sliding of the 553 mm thick PHOS modules into their position at central rapidity at the same final distance to the beam axis. The PHOS modules are so much thicker because they have somewhat higher total radiation lengths but also because all of the readout electronics, not just the photo sensor, is contained within the module enclosure. As a consequence of these 2 heights of aluminium rails, the DCal super modules will have standard carriages for motion in the z-direction on C side, and custom carriages on A-side which elevate them to the same level as the C-side DCal super modules and the same level as the front face of the PHOS modules. To permit access to the back face of the PHOS modules which is required to service the readout electronics, the section of the extruded aluminium rails located directly behind the PHOS module can be removed after installation. In figure VI.8, these rail sections have been removed.

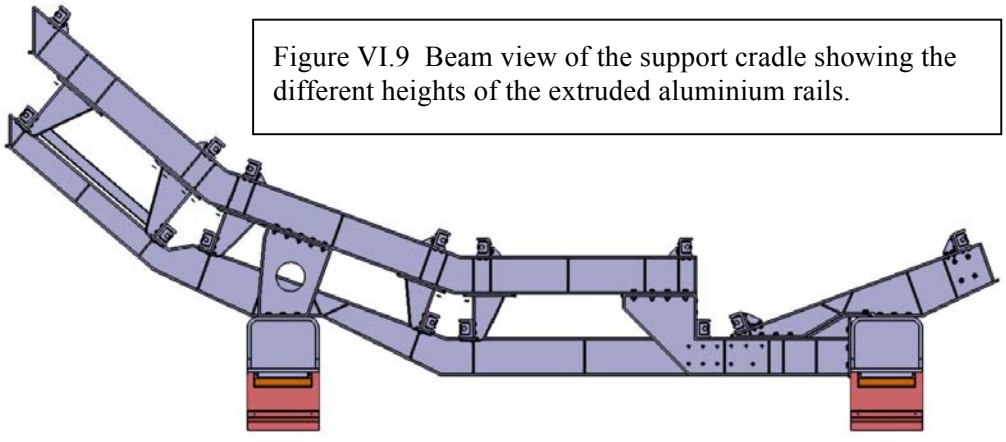

Figure VI.9 Beam view of the support cradle showing the different heights of the extruded aluminium rails.

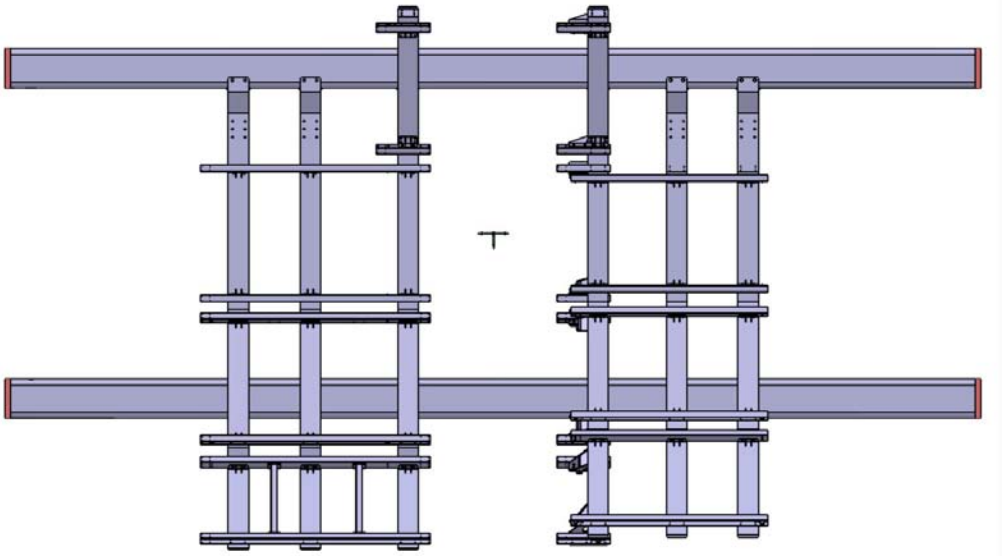

A side Top view C side

Figure VI.10 Top view of the support cradle showing the situation with the section of the extruded aluminium rail directly behind PHOS removed to allow access to PHOS electronics. This is the situation, which applies after PHOS modules are installed.

Figures VI.9 and VI.10 show beam views and top views of the cradle respectively. The beam view shows the upper aluminium extruded rails used for installation and final positioning of the C-Side DCal modules and the lower rails which perform the same function for the PHOS and the A-Side DCal Modules. Figure VI.10 shows the stubs of lower aluminium rails that are left in place to support the PHOS Modules after the modules are fully installed and the central section is removed. Figure VI.11 shows the bottom view of the fully integrated detector.

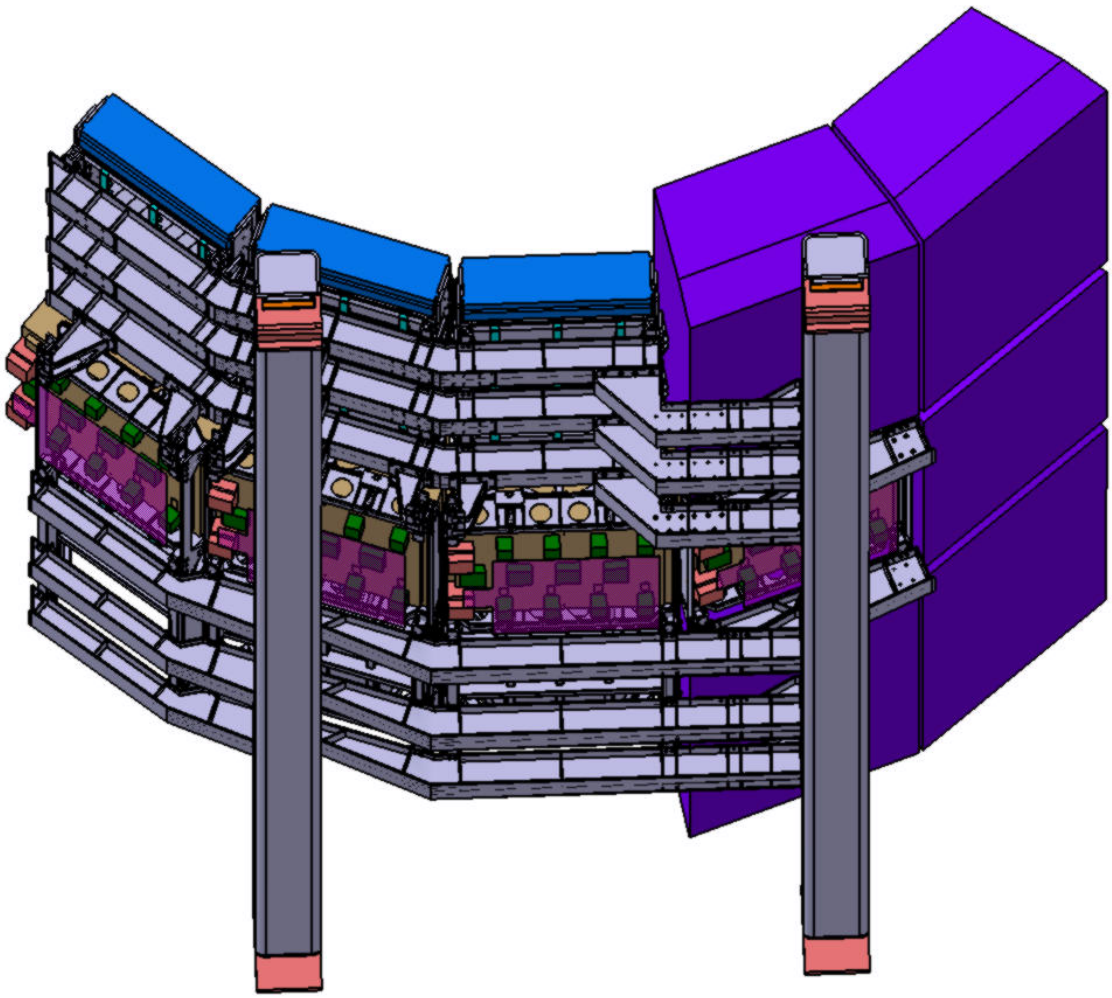

Figure VI.11 Underside view of the fully integrated detector. Access to PHOS electronics is completely open and includes 877 mm clearance to floor under C side ribs. This improves the present access to PHOS.

VI.4.3 Support Cradle Finite Elements Calculations

Calculations were done on single ribs with ANSYS application. The results are shown in figures VI.12 and VI.13 for an A-Side and C-Side rib respectively. The maximum stress on the A-Side is 147MPa with a maximum deflection of 3.6mm. The maximum stress on the C-Side is 159 MPa with a maximum deflection of 4.7mm. In both cases the maximum stress is well below the allowable limit of 245 MPa.

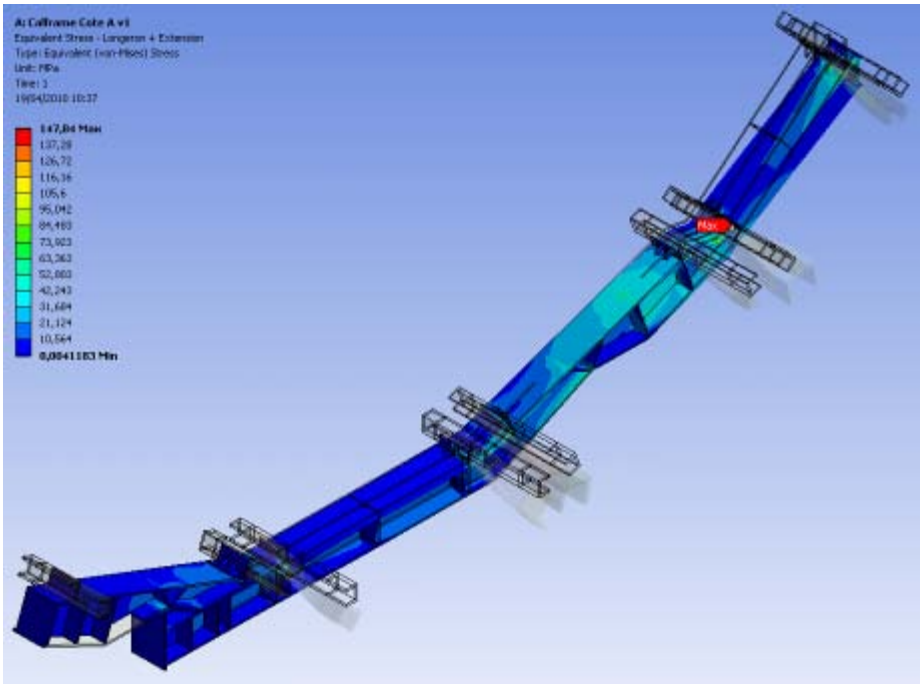

Figure VI.12 Side A rib and sections of the lower rails. The maximum stress is 147 MPa and the maximum deflection is 3.6 mm

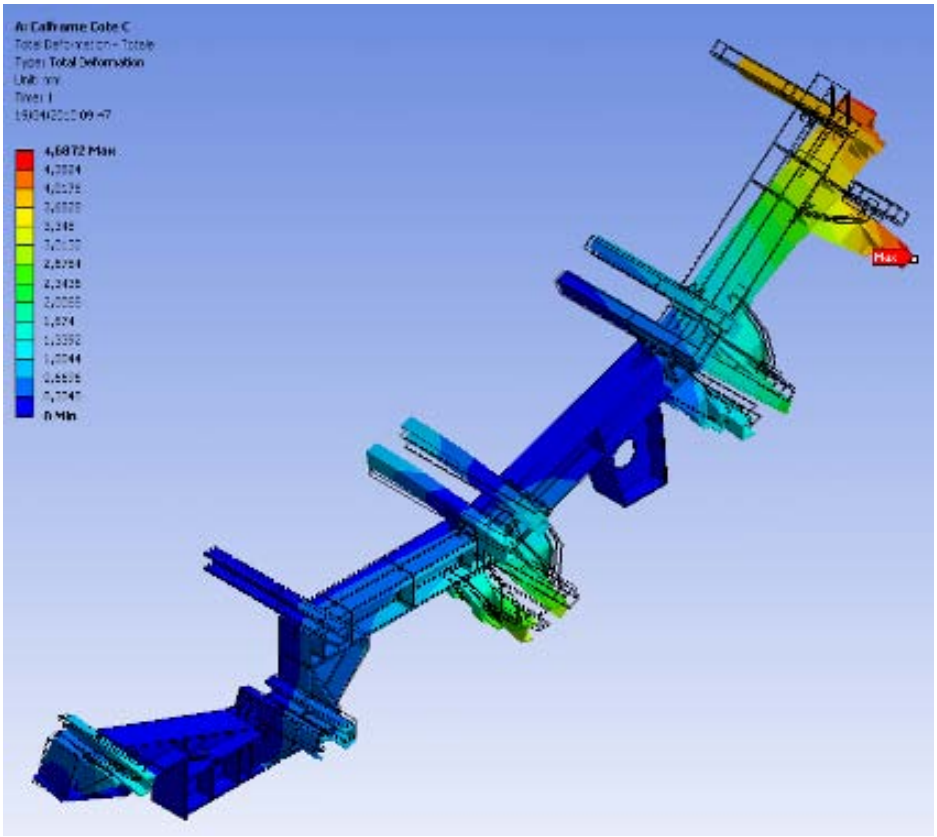

Figure VI.13 Side C rib and sections of both the lower and upper rails. The maximum stress is 159 MPa and the maximum deflection is 4.7 mm

VI.5 DCal and PHOS Installation

The detector installation process begins with C-Side DCal super modules. The super module, mounted on an elevated chariot and inserted into the installation tool, is lifted by crane into the area adjacent to the mini frame (Figure VI.4) at the entrance to the L3 magnet and moved transverse to the beam axis on temporary trails into position as shown in figure VI.14. These temporary transverse rails provide full access to the area beneath the mini frame. During this process, the installation tool has previously been rotated to the correct phi angle for insertion.

The installation process for this super module is then illustrated in the simplified drawing shown in figure VI.15. The super module on its elevated chariot is moved along the lower, A-Side rails and mates at the proper height with the higher C-Side rails. Once the super module is fully in place on the C-Side cradle, the elevated chariot is withdrawn.

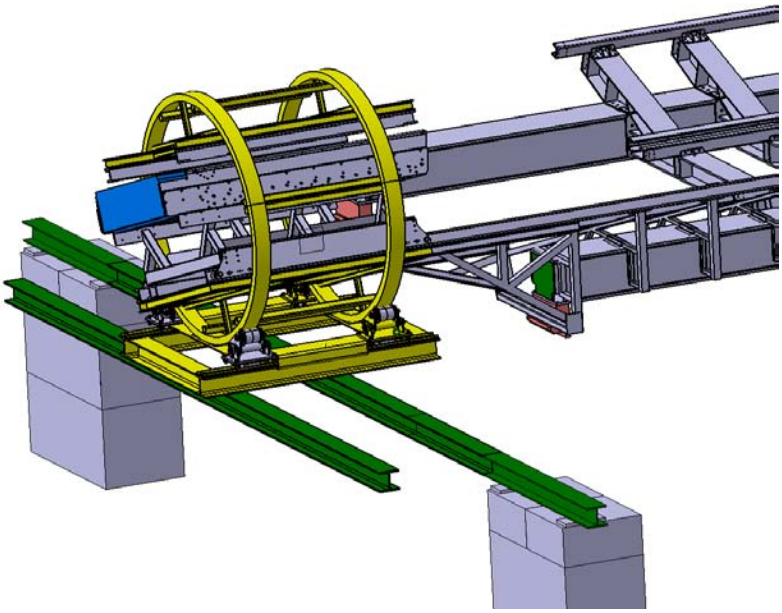

Figure VI.14 A C-Side DCal super module is positioned in the installation tool mounted on an elevated chariot . A custom bridge piece connects the extruded aluminum rails on the A-Side cradle to corresponding rail pieces on the installation tool.

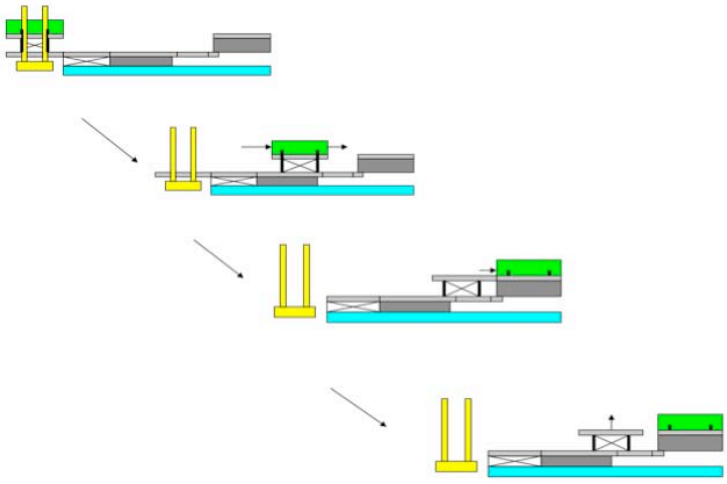

Figure VI.15 A cartoon to illustrate the transfer of a C-Side super module on an elevated chariot from the installation tool across the A-Side cradle to its final position on the C-Side. The elevated chariot is then removed.

Figure VI.16 now illustrates the installation of a PHOS module. The same installation tool is used and again a short bridge piece connects the rails on the installation tool to those on the A-Side cradle. The PHOS module moves along the A-Side rails on a low chariot designed to ensure that the alignment of the front face of the module with the front face of the C-Side DCal super modules. The final positions of the PHOS modules will be identical to those occupied at present. Once the PHOS module is in place, the short segments of aluminium rails between the A-Side cradle and the C-Side cradle is removed to provide unobstructed access to the PHOS electronics.

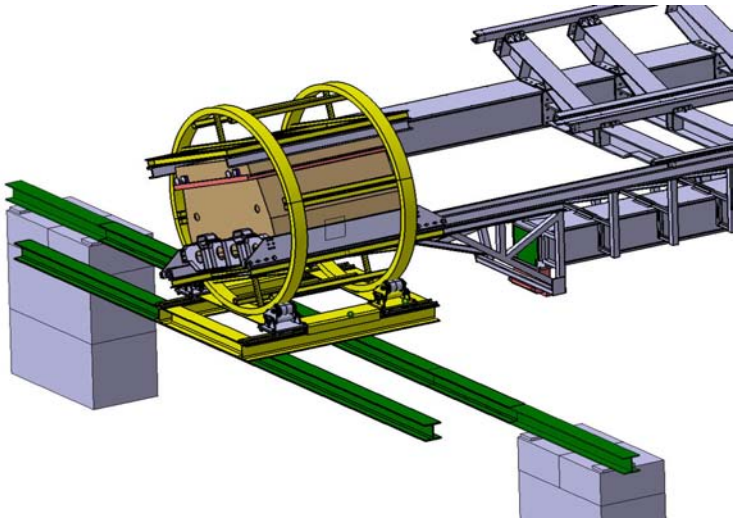

Figure VI.16 A PHOS module is positioned in the installation tool mounted on a low chariot. A custom bridge piece connects the extruded aluminum rails on the A-Side cradle to corresponding rail pieces on the installation tool.

After PHOS module insertion, the charge particle veto (CPV) detectors can be installed. These detectors are used in conjunction with PHOS to increase the sensitivity of the very high resolution PHOS detector. Figure VI.17 illustrates a CPV installation in the presence of one of the C-Side DCal super modules.

Finally the A-side DCal super modules are installed. This is accomplished exactly as shown in figure VI.14 with the exception that the elevated chariot is left in place as the permanent support of the A-Side super module.

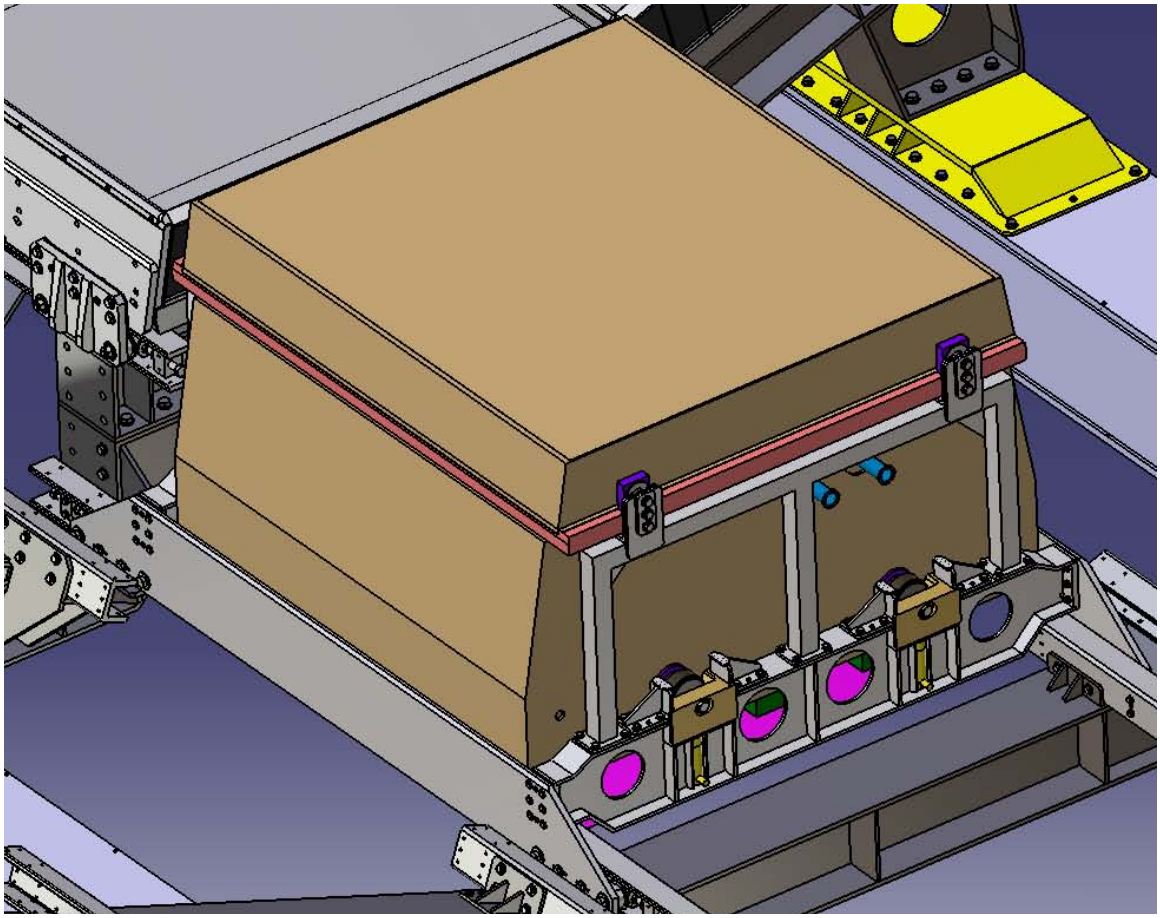

Figure VI.17 A PHOS module with the CPV in place

VII. Scope of the full DCal project and division of responsibilities

The full scope of the DCal project includes 6 super modules, all of their associated readout and trigger systems, all the associated mechanical and electrical integration and the support structure for both PHOS and DCal super modules. In addition, the project includes installation tooling and the required engineering oversight as well as costs associated with DAQ, DCS and HLT integration.

A large fraction of the responsibility within the project is described in terms of the number of super modules contributed by a particular national group. By definition, a super module is taken to include in addition to the mechanically integrated super module, all of its read out, triggering and LED calibration system. Certain of the project costs, however are common to all super modules. By agreement within the collaboration, individual national groups will share these common costs in proportion to the number of super modules they provide.

In detail, common costs within the DCal project include HV and LV supplies and cabling, cable tray modifications, internet connectivity, DAQ communication fibers and communication electronics, DCS integration costs, HLT expansion costs, electronics racks and cooling, expenses associated with re-working existing ALICE cabling and services. In addition, the largest single common cost is design and fabrication of the DCal support structure and installation tooling. The Nantes / SUBATECH group has already assumed responsibility for the design and mechanical analysis of the support structure and installation tooling. At this point, the design and analysis work is completed and reviewed as described above. IN2P3 has indicated its willingness to fund approximately 2/3 of the total fabrication cost of the support structure. The balance of the fabrication cost, possibly not supported by IN2P3 at this point is counted as a common cost.

Given the leading role assumed by our French colleagues in the support structure, we arrive at the distribution of responsibilities given in Table VII.1.

Table VII.1 Individual group responsibilities for the major national groups participating in DCAL.

Group	Group Leader	Proposed Responsibilities
China	D. Zhou. Wuhan	1 super module
Finland	J. Rak, Jyväskylä	TRU, trigger commissioning
France	C. Roy, IPHC Strasbourg	Detector design 0.5 super module Support structure design, fabrication oversight and payment of a minimum of 2/3 the cost Installation tooling design Installation oversight Jet trigger design, hardware and integration SM integration and cosmic calibration
Italy	N. Bianchi, Frascati	Module assembly facilities and oversight Fiber production facilities and oversight APD calibration and preparation facility and oversight
Japan	Y. Miake, Tsukuba	1.5 super modules
Switzerland	H. Muller, CERN	Electronics and trigger design
USA	T.M. Cormier, WSU and LBNL	3 super modules Detector design Project management Technical coordination DCal LED fiber system Electronics oversight and commissioning

The above table does not describe in detail the common responsibilities and associate common costs. Those are assumed and distributed as described in the text.

Most of the national groups participating in DCal were leading participants in the ALICE EMCal. The Japanese and Chinese groups, however, are new to the module production activities that have become routine in the US, France and Italy during the EMCal project. Because time is short to the start-up of DCal production, both Japanese and Chinese technicians and engineers will undergo extensive training at existing EMCal assembly facilities. Specialized assembly tooling required by the Chinese and Japanese in order to participate in module assembly will be provided by Frascati and Catania, Subatech and Wayne State either on site at the EMCal laboratory or shipped directly for use on site in Tsukuba and/or Wuhan.

The participating national groups agree to make every effort to carry out their responsibilities outlined in Table VII.1.

VIII. Project cost and schedule

The CORE project cost and schedule is given in Tables VIII.1 and VIII.2 respectively

DCAL System	Estimated Cost (kCH) 6 Supermodules
Mechanical Components production	1,744
Electronics Production	1,047
DCal Service Integration	174
Rails and Support Structure	436
Insertion Tooling	140
Total Shipping Cost	419
DCal total cost	3,959

Table VIII.1 Major cost items of the DCal project. Costs are presented in kCH and assume present exchange rates across the several currencies used within the project.

The cost estimate is based on over two years of experience with the EMCal project construction or vendor quotes in the case of the few new components. The cost does not include labor or detector R&D. Specialized module assembly tooling all of which was produced as part of the EMCal project is not included in the cost. At the present time, all of these cost elements are funded by the participating funding agencies at the level indicated.

The schedule indicated in table VIII.2 is aggressive but given EMCal experience it is realistic. Project scheduling aims to have as much as DCal as possible ready and delivered to CERN point-2 for the long 2011 shutdown.

ID	Task Name	Finish
1	**DCal Supermodule No. 1 Ready for Installation**	**Fri 2/18/11**
2	**DCal Integration Into Alice**	**Fri 2/18/11**
3	Support Rails Design	Fri 4/30/10
4	Support Cradle Design	Fri 4/30/10
5	Insertion Tooling Preliminary Design	Fri 4/30/10
6	Dcal Utilities/Services Integration Preliminary Design	Fri 4/30/10
7	Design Review	Tue 5/25/10
8	Rails Material Procurement	Mon 9/13/10
9	Rail Fabrication	Mon 12/6/10
10	Rails Available for Installation	Mon 12/6/10
11	Support Cradle Farication	Mon 1/3/11
12	Support Cradle Ready for Installation	Mon 1/3/11
13	Insertion Tooling Final Design	Fri 9/17/10
14	Insertion Tooling Fabrication	Fri 1/7/11
15	Utilities/Services Integration Final Design	Fri 8/20/10
16	Utilities/Services Fabrication	Fri 11/12/10
17	Services Ready for Installation	Fri 11/12/10
18	DCal Integration Is Ready	Mon 1/3/11
19	**DCal Supemodule Production**	**Fri 2/18/11**
20	Material Procurement	Fri 7/23/10
21	Module Assembly in Japan	Fri 11/12/10
22	Module Assembly in China	Fri 1/7/11
23	Module Assembly in France	Fri 10/15/10
24	StripModule Assembly In Nantes	Fri 2/4/11
25	Module and Stripmodule production at WSU	Fri 1/7/11
26	Dcal SM No. 1 Assembly at Grenoble (USA)	Fri 10/15/10
27	DCal Supermodule No. 1 Ready for Installation	Fri 10/15/10
28	Dcal SM No. 2 Assembly at Grenoble (Japan)	Fri 12/10/10
29	DCal Supermodule No. 2 Ready for Installation	Fri 12/10/10
30	Dcal SM No. 3 Assembly at Grenoble (USA)	Fri 12/10/10
31	DCal Supermodule No. 3 Ready for Installation	Fri 12/10/10
32	Dcal SM No. 4 Assembly at Grenoble (Japan-Fran	Fri 1/28/11
33	DCal Supermodule No. 4 Ready for Installation	Fri 1/28/11
34	Dcal SM No. 5 Assembly at Grenoble (USA)	Fri 2/4/11
35	DCal Supermodule No. 5 Ready for Installation	Fri 2/4/11
36	Dcal SM No. 6 Assembly at Grenoble (China)	Fri 2/18/11
37	DCal Supermodule No. 6 Ready for Installation	Fri 2/18/11
38	**Dcal Supermodule Production Is complete**	Fri 2/18/11

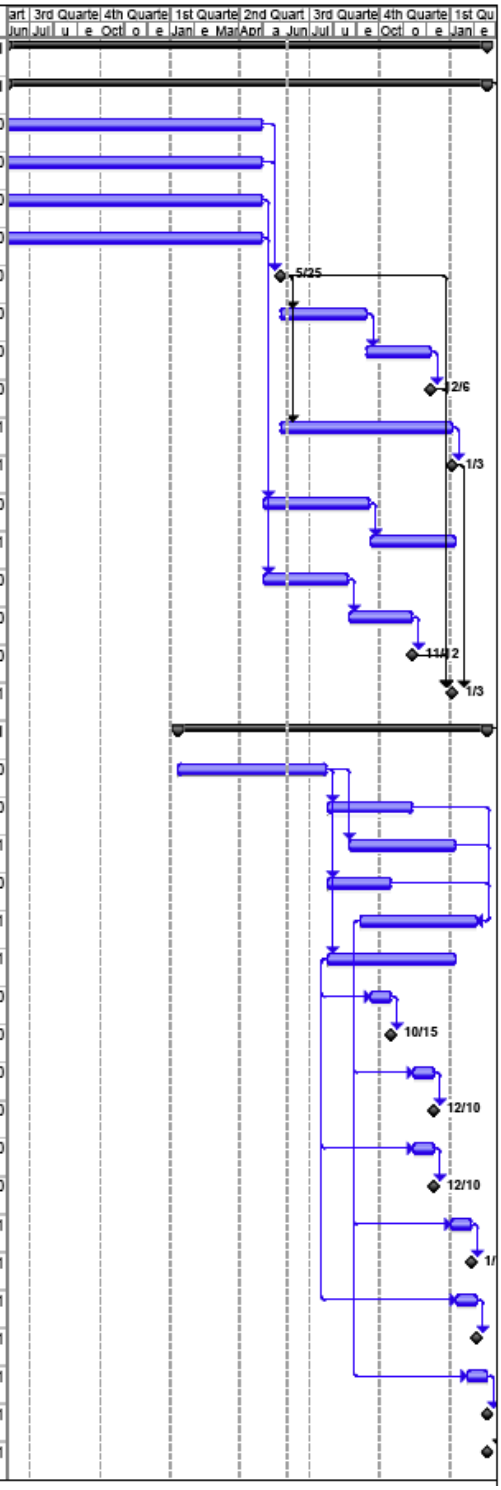

Table VIII.2 DCal project schedule. Under the conditions assumed for project start up a completion date of February 2011 is projected